Evolution of an MHD-scale Kelvin-Helmholtz vortex accompanied by magnetic reconnection: Two-dimensional particle simulations

T. K. M. Nakamura,[1] H. Hasegawa,[1] I. Shinohara,[1] and M. Fujimoto[1]

[1]   We have performed 2.5-dimensional full particle simulations of an MHD-scale Kelvin-Helmholtz (KH) vortex and accompanying magnetic reconnection. This is the first study of so-called vortex-induced reconnection (VIR) using kinetic simulations. First, as a key property of the VIR, we found that magnetic reconnection occurs at multiple points in the current sheet compressed by the flow of the KH vortex. The resulting multiple mesoscale islands are carried toward the vortex body along the vortex flow and then are incorporated into the vortex body via re-reconnection. The rates of the first reconnection and second re-reconnection are both generally higher than that of spontaneous reconnection; both reconnection processes are of driven nature. Noteworthy is that the high rate of the first reconnection leads to strong magnetic field pileup within the multiple islands. This characteristic magnetic structure of the islands could be used as new observational evidence for the occurrence of the VIR. Next, as a key kinetic aspect of the VIR, we found that a series of the multiple island formation and incorporation processes causes efficient plasma mixing in real space and bidirectional magnetic field-aligned acceleration of electrons simultaneously within the vortex. These kinetic effects of the VIR could account for observed features of the Earth's low-latitude boundary layer, where mixed ions and bidirectional field-aligned electrons generally coexist.
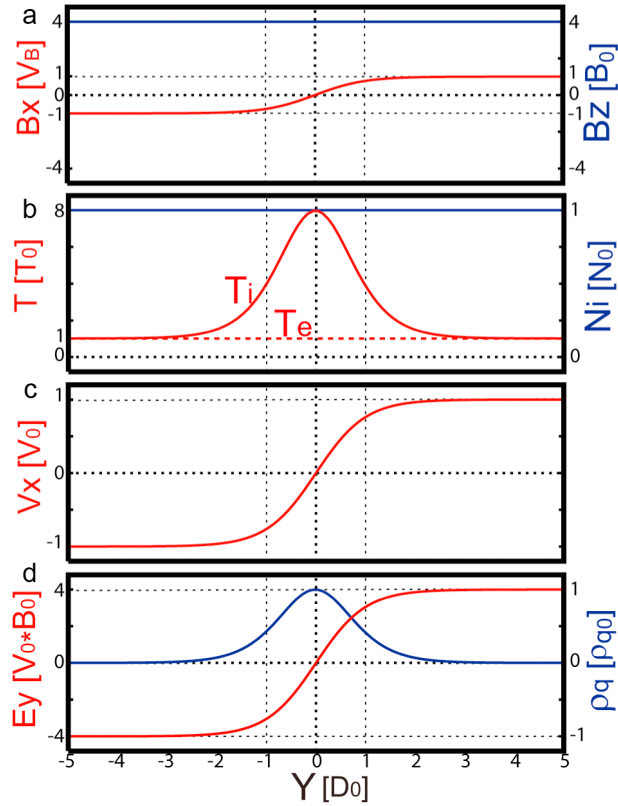
1. Introduction

[2]   The Kelvin-Helmholtz instability (KHI) has been considered as one of the most important processes for momentum and energy transport or plasma transport and mixing in collisionless space plasma systems, such as planetary magnetopause boundary layers [e.g., *Dungey*, 1955; *Miura*, 1984; *Fujimoto and Terasawa*, 1994; *Nykyri and Otto*, 2001; *Nakamura et al.*, 2008, 2010]. The KHI is a well-known hydrodynamic instability that grows in a velocity shear layer [e.g., *Chandrasekhar*, 1961], one example of which is the Earth's magnetopause situated between the shocked solar wind and stagnant magnetospheric plasma. Indeed, around the Earth's low-latitude magnetopause, KH wave-like quasi-periodic fluctuations have been frequently observed when the interplanetary magnetic field (IMF) direction is northward [e.g., *Sckopke et al.*, 1981; *Fairfield et al.*, 2000]. Moreover, clear evidence of rolled-up vortices, believed to result from the nonlinear development of the KHI, has recently been found from observations by the Cluster spacecraft around the magnetopause during northward IMF [*Hasegawa et al.*,

2004a]. Also at the Mercury's magnetopause, vortex-like magnetic structures that may be produced by the KHI have recently been encountered by MESSENGER during its first and third flybys of Mercury [*Slavin et al.*, 2008, 2009; *Boardsen et al.*, 2010].

[3]   Earthward of the Earth's low-latitude magnetopause, there is a boundary layer that contains a mixture of plasmas of solar wind (magnetosheath) and magnetosphere origins [e.g., *Sckopke et al.*, 1981; *Mitchell et al.*, 1987; *Fujimoto et al.*, 1998; *Hasegawa et al.*, 2003]. This so-called low-latitude boundary layer (LLBL) tends to become thicker with downtail distance when the IMF direction is northward [*Mitchell et al.*, 1987; *Hasegawa et al.*, 2004b]. While the formation mechanism of the LLBL under northward IMF is still under debate [e.g., *Song and Russell*, 1992; *Phan et al.*, 1997], the KH vortex excited at the low-latitude magnetopause is believed to play some key roles [e.g., *Sckopke et al.*, 1981; *Chaston et al.*, 2007; *Nakamura et al.*, 2008].

[4]   In order to understand how the KH vortex could cause plasma mixing across the magnetopause and eventually form the LLBL, a number of numerical simulations have been performed [e.g., *Miura*, 1984; *Otto and Fairfield*, 2000; *Nakamura et al.*, 2004, 2008]. Since the KH waves tend to be observed during northward IMF, several numerical simulations have been performed for the simple transverse case, in which the magnetic field direction is strictly perpendicular to the shearing flow direction, that is, only northward magnetic

[1]Institute of Space and Astronautical Science, JAXA, Sagamihara, Japan.

Figure 1. (a–d) Initial profiles of the in-plane magnetic field component (B_X), out-of-plane magnetic field component (B_Z), ion and electron temperatures (T_i and T_e), ion density (N_i), bulk flow velocity (V_X), convective electric field (E_Y), and net charge density $\rho_{q0} = 1/4\pi[\nabla \cdot E]_{max}$.

netic field component, parallel to the initial flow direction. It is shown that the dynamics of KH vortices is affected significantly by this in-plane component [e.g., *Chandrasekhar*, 1961; *Miura and Pritchett*, 1982]. The in-plane magnetic field tends to suppress the linear growth of KHI [*Miura and Pritchett*, 1982] as well as the formation of a fully rolled-up vortex [*Nakamura and Fujimoto*, 2005]. Since the growth of secondary vortices as mentioned above also tends to be suppressed by the in-plane magnetic field component, the plasma mixing via secondary vortices would not take place in actual situations [*Nakamura et al.*, 2008]. However, the in-plane field lines may be highly deformed by the vortex flow and then can be reconnected [e.g., *Pu et al.*, 1990; *Nykyri and Otto*, 2001; *Knoll and Chacón*, 2002; *Chacón et al.*, 2003; *Nakamura and Fujimoto*, 2008; *Nakamura et al.*, 2008]. This so-called vortex-induced reconnection (VIR) can lead to direct mixing and transport of plasma across the shear layer. *Nakamura et al.* [2008] have summarized the properties of two types of VIR.

[6] 1. Type I occurs when the in-plane field is initially antiparallel across the shear layer (antiparallel case) so that a current sheet is embedded in the shear layer [e.g., *Pu et al.*, 1990; *Knoll and Chacón*, 2002; *Nakamura et al.*, 2006]. This type of VIR is induced at the hyperbolic point where the vortex flow locally compresses the current sheet. Noteworthy is that type I VIR can cause plasma mixing in real space across the shear layer along reconnected field lines.

[7] 2. Type II is driven only when the velocity shear is strong enough to produce highly rolled-up KH vortices and thus to overcome the in-plane magnetic tension [e.g., *Nykyri and Otto*, 2001; *Nakamura and Fujimoto*, 2005]. In the type II case, the field lines that have been amplified and stretched by the strong rolling-up flow are reconnected.

[8] *Nakamura et al.* [2008] have also revealed, based on linear analysis, that the KHI tends to grow in the plane where the in-plane field becomes antiparallel across the shear layer. It means that the KH vortex growing at the magnetopause could be almost always accompanied by type I VIR. Thus, type I VIR could play a key role in the plasma mixing across the magnetopause and, as a result, the LLBL formation. Indeed, direct evidence of type I VIR at the Earth's magnetopause has recently been found from Cluster data [*Hasegawa et al.*, 2009]. *Hasegawa et al.* [2009] also reported that around the type I VIR region, electrons are accelerated along the magnetic field lines. While this result clearly shows the importance of kinetic effects of type I VIR on the plasma mixing and particle acceleration, no kinetic simulations of type I VIR have been performed to date. This study presents the first full particle simulations to investigate kinetic properties of type I VIR. Our new results show that type I VIR generally involves the formation of multiple magnetic islands (section 3). Further, this islands formation can lead to fast plasma mixing within the vortex and strong electron acceleration along the reconnected field lines (section 4). Since these kinetic properties are similar to those seen in the Earth's LLBL, our particle simulation results

field component is present [e.g., *Miura*, 1984, 1987; *Nakamura et al.*, 2004; *Matsumoto and Hoshino*, 2006; *Cowee et al.*, 2009]. *Miura* [1984, 1987] revealed using two-dimensional MHD simulations that efficient momentum transport across the magnetopause is caused by KH vortices. Plasma mixing, however, cannot take place under the frozen-in condition assumed in the ideal MHD. On the other hand, recent two-dimensional two-fluid (proton and electron fluids) simulations including finite electron inertial effects have shown that when a moderate density jump exists across the initial velocity shear layer, rolled-up KH vortices are destroyed via small-scale secondary vortices excited along the edge of the parent vortex [*Nakamura et al.*, 2004]. Recent particle simulations have further confirmed that such a decay process via secondary vortices causes efficient plasma mixing within the KH vortex [*Matsumoto and Hoshino*, 2006; *Cowee et al.*, 2009].

[5] While the above numerical studies considered only the out-of-plane (perpendicular) magnetic field component, actual velocity shear layers commonly have in-plane mag-

Table 1. Simulation Parameters

	m_i/m_e	ω_{pe}/Ω_e	T_{csi}/T_{bgi}	T_{cse}/T_{bge}	T_{bgi}/T_{bge}	V_{thi_bg}	V_{Ai}	λ_i	n_0/cell
Value	25	2.0	8	1	1	0.033c	0.1c	16dx	100
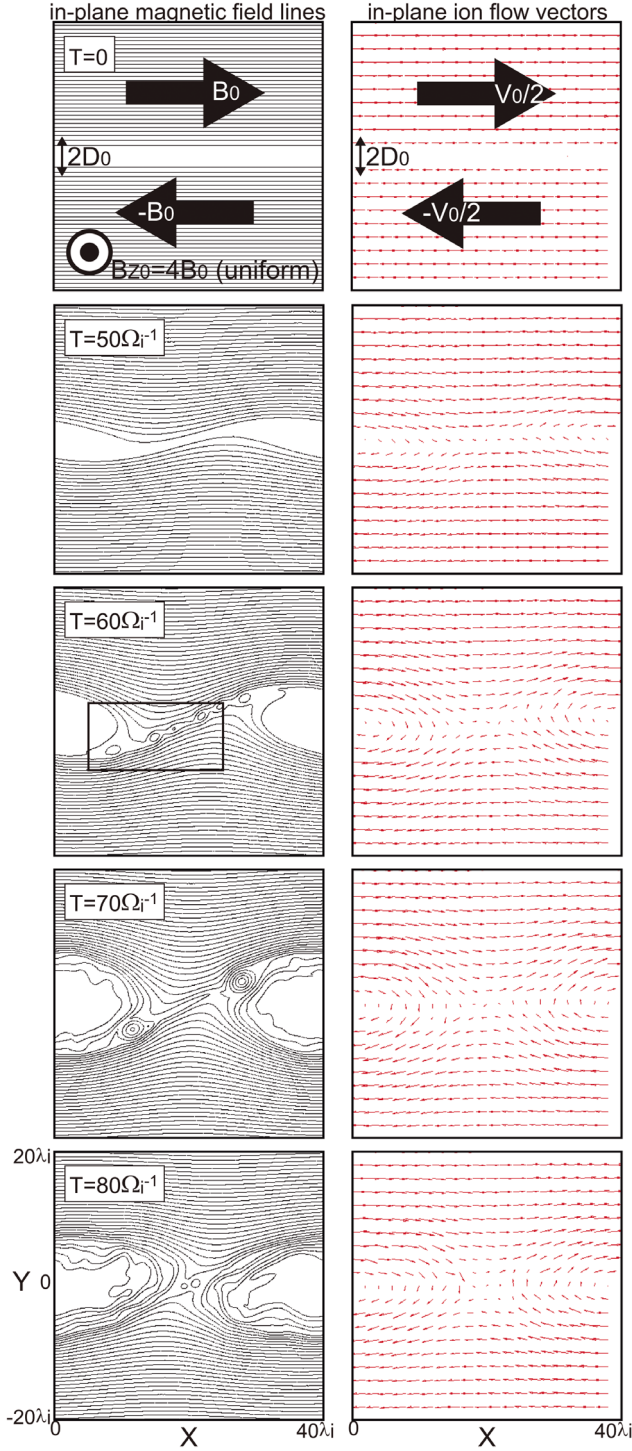
Figure 2. Time series of (left) in-plane magnetic field lines and (right) in-plane ion flow vectors in the $D_0 = 2.0\lambda_i$ and $M_A = 4.375$ case.

could provide an explanation for the LLBL formation process, as discussed in section 5.

[9] This paper is organized as follows. Section 2 details the simulation setting. Section 3 presents an overview of our simulation results and fundamental properties of type I VIR.

Section 4 presents kinetic roles played by type I VIR in the fast plasma mixing and strong electron acceleration. Finally, in section 5, we summarize the results and discuss applications of the results. In the rest of the paper, type I VIR is referred to simply as the VIR.

2. Simulation Setting

[10] We perform 2.5-dimensional (two spatial dimensions and three vector components) relativistic electromagnetic particle simulations which retain the full dynamics of the constituent particles. In this study, we consider protons (hereafter called "ions") and electrons as the particles. Details of the simulation method are described by *Nakamura et al.* [2010].

[11] Figure 1 shows the initial profiles of the in-plane and out-of-plane magnetic field components, ion density, ion and electron temperatures, bulk flow velocity, convective electric field, and net charge density normalized by the maximum initial charge density $\rho_{q0} = 1/4\pi[\nabla \cdot E]_{\max}$. In this study, we focus on fundamental situations in which the initial ion density n_{i0} is uniform (Figure 1b). In order to form the velocity shear layer, particles are initialized with shifted Maxwellian velocity distributions having a bulk velocity $V_{X0} = V_0/2 \cdot \tanh(Y/D_0)$, where D_0 is the initial half thickness of the shear layer and V_0 is the initial velocity jump across (Figure 1c). The initial in-plane magnetic field component is strictly antiparallel across the shear layer with $B_{X0} = B_0 \cdot \tanh(Y/D_0)$, and the initial out-of-plane magnetic field component is uniform with $B_{Z0} = 4B_0$ (Figure 1a). In order to maintain the total pressure balance, the initial ion temperature at the center of the shear layer (the current sheet) is set to be 8 times the background ion temperature ($T_{csi}/T_{bgi} = 8$), whereas the electron temperature is uniform ($T_{cse}/T_{bge} = 1$) (Figure 1b). The background ion-to-electron temperature ratio is set at $T_{bgi}/T_{bge} = 1$ (Figure 1b). The convective electric field $E_{Y0} = -V_{X0} \cdot B_{Z0}$ is set to sustain the shear flow. Since the nonuniform convective electric field breaks the charge neutrality (Figure 1d), in our simulations electrons are loaded slightly nonuniformly to satisfy Gauss's law [*Pritchett and Coroniti*, 1984].

[12] Table 1 summarizes the initial simulation parameters used in this study. The ion-to-electron mass ratio M is set to be $M = m_i/m_e = 25$. The ratio between the electron plasma frequency and the gyrofrequency is set at $\omega_{pe}/\Omega_e = 2.0$. The ion thermal and ion Alfvén speeds are set to be $V_{thi} = 0.033c$ and $V_{Ai} = 0.1c$, respectively. Here c is the light speed. The size of the spatial grid dx is set to be slightly shorter than the electron Debye length λ_{De}. The average number of particles per cell is $n_0 dx^2 = 100$. The ion inertial length λ_i is set to be 16dx. The system is periodic in the X direction with its size almost equal to the wavelength of the fastest growing KH mode $L_X = \lambda_{KH}$ (=$20D_0$) [*Miura and Pritchett*, 1982], and the conducting walls are located at $Y = \pm L_X$. The initial half thickness of the shear layer (the current sheet) is varied in the range of $\lambda_i \leq D_0 \leq 4\lambda_i$, and the initial velocity jump V_0 in the range of $2.5V_{Ai} \leq V_0 \leq 5V_{Ai}$, that is, 2.5 (weak KHI) $\leq M_A \leq 5$ (strong KHI). Here V_{Ai} and $M_A = V_0/V_{Ai}$ are the Alfvén speed and the Alfvén Mach number, respectively. All V_{Ai} and M_A used in this paper are based on the in-plane magnetic field component. (Past linear analyses show that the KHI can grow to overcome the magnetic field tension
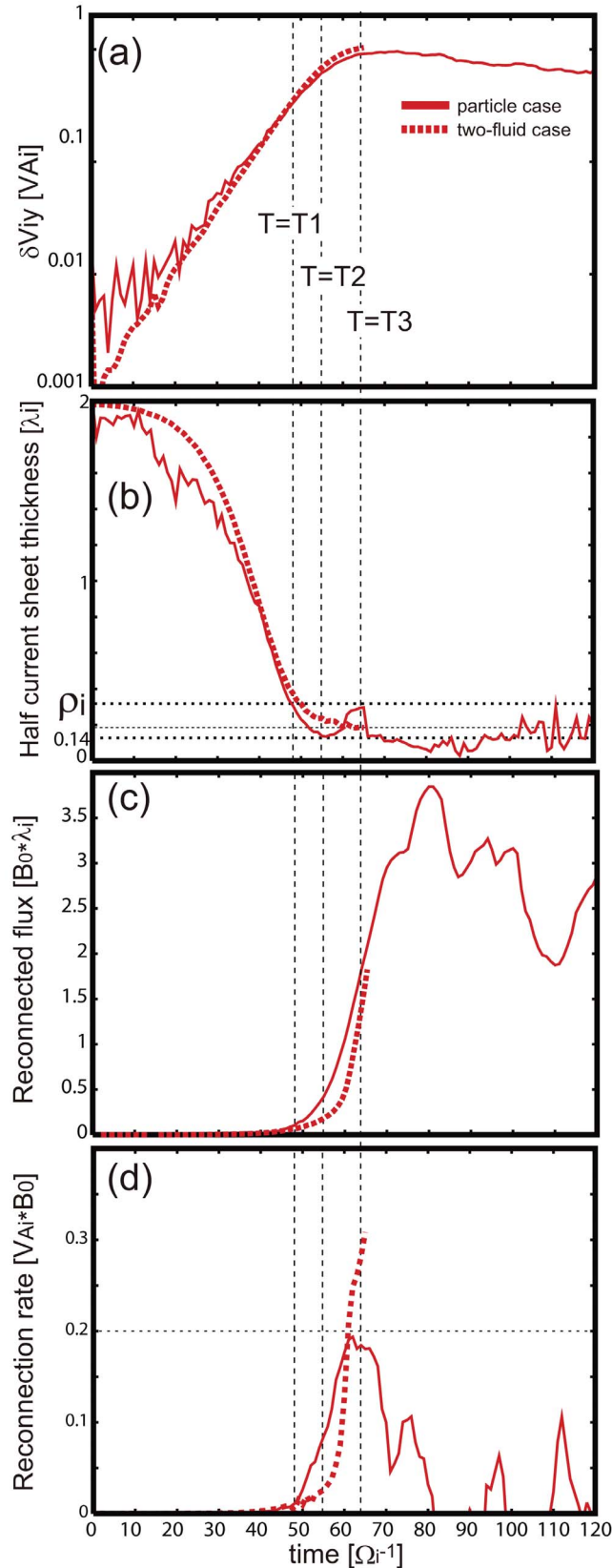
when $M_A > 2$ [*Miura and Pritchett*, 1982].) To initiate the KH mode we add a small flow perturbation $\delta V_{iy} = \delta V_{ey} = \delta V_0 \cdot V_0 \exp[-(Y/D_0)^2] \cdot \sin(2\pi X/L_X)$. Here δV_0 is the amplitude of the initial perturbation, which is set to be 0.02.

[13] Note that when $V_0'(Y)/\Omega_i \ll 1$ (the so-called weak shear case), in addition to the KHI, an ion wave could be excited around the ion cyclotron frequency Ω_i due to the convective electric field [e.g., *Ganguli et al.*, 1988; *Opp and Hassam*, 1991]. Here $V_0'(Y) = dV_0(Y)/dY$. In addition, when the initial half thickness of the shear layer is less than ion Larmor radius ($D_0 < \rho_i$), the structure of the shear layer and associated KHI growth are largely affected by the ion Larmor radius effect [*Cai et al.*, 1990; *Nakamura et al.*, 2010]. Therefore, in order to investigate effects of reconnection on the KHI under little influence of these ion kinetic processes, we focus only on the strong shear ($V_0'(Y)/\Omega_i \sim 1$) and MHD-scale ($D_0 \geq \lambda_i > \rho_i$) situations.

3. Fundamental Properties of the Vortex-Induced Reconnection

3.1. Overview of the Vortex-Induced Reconnection

[14] Figure 2 shows a time series of in-plane magnetic field lines (Figure 2, left) and in-plane ion flow vectors (Figure 2, right) in the $D_0 = 2.0\lambda_i$ (MHD-scale) and $M_A = 4.375$ (strong KHI) case. Once the KHI begins to grow, the flow of the KHI compresses the current sheet around the hyperbolic point toward which the vortex flow converges ($T = 50\Omega_i^{-1}$). Then, magnetic reconnection is induced at multiple points in the compressed current sheet, and consequently multiple magnetic islands are formed ($T = 60\Omega_i^{-1}$). These islands are carried toward the vortex body along the vortex flow and are incorporated into the vortex body in turn via re-reconnection ($T = 70\Omega_i^{-1}$). Finally, the KH vortex is highly rolled up to end up as a large magnetic island ($T = 80\Omega_i^{-1}$).

[15] Red solid lines in Figure 3 show the Y component of the ion velocity δV_{iY} for the KH mode with m = 1, half thickness of the compressed current sheet, reconnected magnetic flux, and the reconnection rate. δV_{iY} is calculated by the Fourier series expansion of V_{iY} at $Y = 0$. The current sheet thickness is calculated from the maximum absolute value of the Z component of the current density $|J_Z|_{max}$ and the in-plane magnetic field intensity at the edge of the current sheet $|B_{XY}|_{edge}$ as $d = D_0 \cdot (|J_Z|_{max}/|J_{Z0}|_{max}) \cdot (|B_{XY}|_{edge}/B_0)$. The reconnected flux is obtained from the maximum value of the Z component of the vector potential at the compressed current sheet, and the reconnection rate is defined as time rate of change of the reconnected flux. Note that these reconnected flux and reconnection rate refer to the X point

Figure 3. (a) The Y component of ion velocity δV_{iY} for the m = 1 KH mode, (b) half thickness of the compressed current sheet, (c) reconnected magnetic flux, and (d) the reconnection rate as a function of time in the $D_0 = 2.0\lambda_i$ and $M_A = 4.375$ case. Red solid (dashed) lines show the result of the particle (two-fluid) simulation. T1, T2, and T3 are defined as the time when the current sheet thinning begins to stop, the time when the current sheet thickness reaches a minimum, and the time when the rate of the VIR peaks, respectively, in the particle simulation.
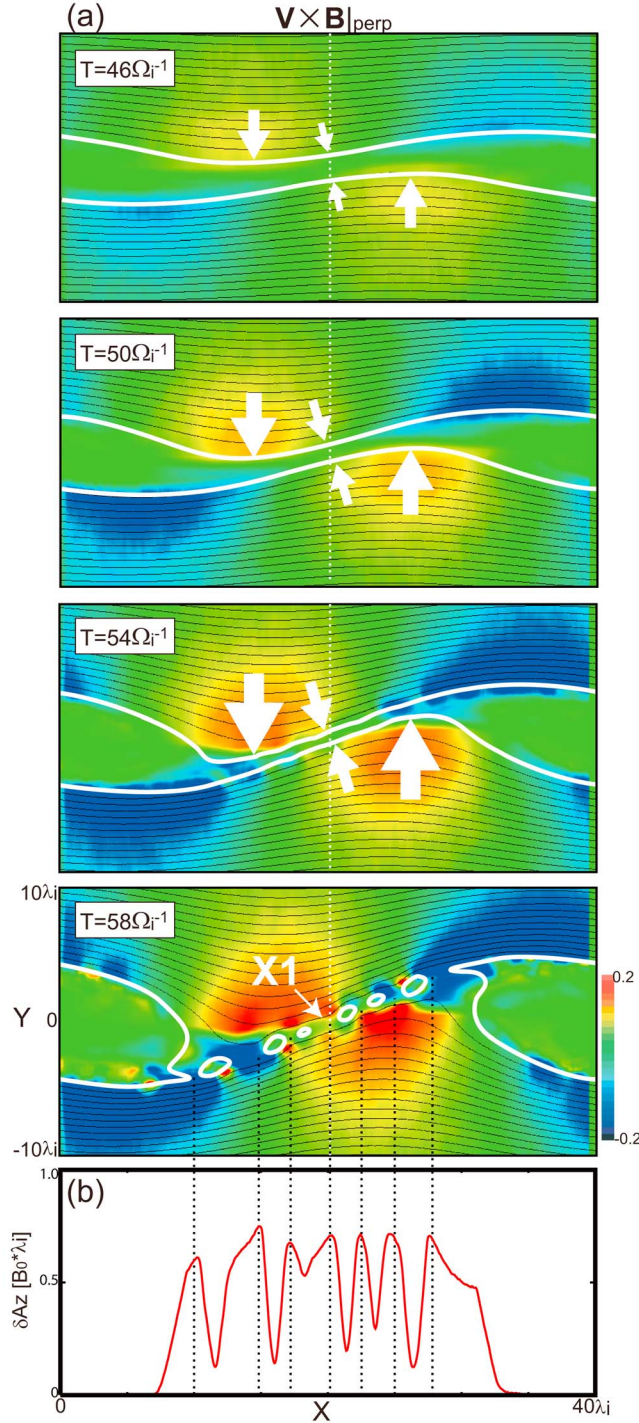
Figure 4. (a) Time series of the convective electric field (shown in color) perpendicular to in-plane magnetic field lines in the $D_0 = 2.0\lambda_i$ and $M_A = 4.375$ case. Black lines show in-plane magnetic field lines, and white lines show the field lines which initially exist at the edges of the shear layer and later reconnect to each other. (b) The δAz along the compressed current sheet at T = $58\Omega_i^{-1}$. Each peak value in Figure 4b corresponds to the reconnected flux at each X point (see text for details).

with the largest reconnected flux and the highest reconnection rate of all X points at each instant. In the linear stage of the KHI, the current sheet becomes thinner with the growth of the KHI (T < $48\Omega_i^{-1}$). At T~$48\Omega_i^{-1}$ (T1), the current sheet thickness reaches the gyroradius of thermal ions, and at the same time reconnection begins to grow rapidly. Just after that, the current sheet thinning stops (T2: T~$55\Omega_i^{-1}$). Finally at T~$65\Omega_i^{-1}$ (T3) the reconnection rate peaks, which coincides with the δV_{iY} peak. The minimum thickness of the current sheet is about $0.14\lambda_i$. This value is small enough to form multiple magnetic islands in the compressed current sheet (see section 3.3 for details). The maximum reconnection rate is about $0.2V_{Ai} \cdot B_0$. This is about twice the typical value (0.1) in the spontaneous reconnection process [e.g., *Birn et al.*, 2001]. It means that the VIR is a kind of driven reconnection. In section 3.2, we will explain how such a high reconnection rate is accomplished.

3.2. Rate of the Vortex-Induced Reconnection

[16] Figure 4a shows a time series of the convective electric field perpendicular to in-plane magnetic field lines in the $D_0 = 2.0\lambda_i$ and $M_A = 4.375$ case. Figure 4b shows δAz ($=|A_Z| - |A_{cs0}|$) along the compressed current sheet at T = $58\Omega_i^{-1}$, which is characterized by the minimum value of $|A_Z|$ at each X coordinate. Each peak value in Figure 4b corresponds to the reconnected flux at each X point. As the KH vortex grows, the vortex flow widely tilts the current sheet, and therefore the current sheet is widely compressed around the hyperbolic point (T~$54\Omega_i^{-1}$). Consequently, reconnection occurs at multiple points in the widely compressed current sheet (T = $58\Omega_i^{-1}$). It is notable here that the reconnected flux is almost equal at all X points (Figure 4b). It means that the reconnection rate at each X point is almost equal to the maximum value shown in Figure 3d. Let us now explain what controls the rate of the VIR, focusing on an X point X1 at the center of the compressed current sheet ($X = 20\lambda_i$) as a representative of the multiple X points. Figures 5a and 5b show the maximum ion flow speed, V_{pmax}, perpendicular to the magnetic field lines on $X = 20\lambda_i$, and in-plane magnetic field intensity $|B_{XY}|$ at the maximum inflow (V_{pmax}) point, respectively. Since X1 moves away from $X = 20\lambda_i$ after T~$65\Omega_i^{-1}$, we here discuss physics of the VIR at X1 for the period before T~$65\Omega_i^{-1}$. Red line in Figure 5c shows the magnetic flux flowing into the point X1, which is computed by $|V_{pmax}|$ (Figure 5a) times $|B_{XY}|$ (Figure 5b). Since the peak of this inflowing magnetic flux corresponds with the peak reconnection rate (T = T3), it can be said that the peak V_{pmax} corresponds to the peak reconnection inflow speed at X1. Furthermore, since V_{pmax} is roughly equal to $\delta V_{iY}/4$ (Figure 5a), it can also be said that the peak reconnection rate is determined by the peak δV_{iY}. Since δV_{iY} at T = T3, δV_{iYmax}, is about $1.0V_{Ai}$ (Figure 3a) and $|B_{XY}|$ at T = T3, B_{inflow}, is about $0.8B_0$ (Figure 5b), the peak reconnection rate can be expressed using V_{Ai} and B_0 as $\delta V_{iYmax}/4 \cdot B_{inflow} \sim 1.0V_{Ai}/4 \cdot 0.8B_0 \sim 0.2V_{Ai} \cdot B_0$. It is therefore concluded that the strong flow of the KH vortex controls the VIR and leads to the high reconnection rate.

[17] Generally speaking, the KHI is saturated at $\delta V_{iY} \sim 0.2V_0 = 0.2M_A \cdot V_{Ai}$. In addition, B_{inflow}, which basically depends on the vortex growth phase, tends to become 0.7–$0.8B_0$ when $\delta V_{iY} \sim 0.2V_0$. As a result, the peak normalized reconnection rate is expected to reach $0.04M_A$. This means

that the rate of the VIR basically depends on M_A only. Indeed, our parametric study in the ranges of $1.0\lambda_i \leq D_0 \leq 4.0\lambda_i$ and $2.5 \leq M_A \leq 5.0$ has confirmed that the peak reconnection rates are always about $0.04M_A$ (partially shown in Figure 6). These results indicate that the rate of the VIR always exceeds 0.1 unless M_A is very close to 2.0 (note that the KHI unstable condition is $M_A > 2$ [*Miura and Pritchett*, 1982]). In other words, the VIR is generally a driven process.

3.3. Multiple Magnetic Island Formation and Merging Processes

[18] Figure 7a shows a time series of the zoom-in view of the region surrounded by the black box in Figure 2. Color contours show the out-of-plane magnetic field component (B_Z). First, the current sheet is widely compressed to the minimum thickness d_{min} of about $0.14\lambda_i$ (T~$50\Omega_i^{-1}$) and subsequently, multiple islands are formed (T~$55\Omega_i^{-1}$). It is noted that the initial length of these islands L_{isnand} is about $1.7\lambda_i$, which is roughly equal to the wavelength of the fastest growing tearing mode excited in the compressed current sheet ($12d_{min}$). This can be explained as follows: the current sheet thinning stops when the outflowing flux that is controlled by the growth rate of the tearing instability comes into balance with the inflowing flux that is controlled by the KHI growth rate (see section 3.4 for details). It means that the time scale of the tearing instability becomes comparable to that of the KHI when the current sheet thickness reaches its minimum. In addition, the current sheet is compressed so widely that its length becomes longer than the wavelength of the fastest growing tearing mode to be excited there. The islands whose typical length is about $12d_{min}$ are therefore formed. A similar island formation process was seen in past particle simulations of driven reconnection [*Pei et al.*, 2001a], although they did not mention in detail the island formation mechanism. After the multiple island formation, these islands are carried along the vortex flow, have high-speed collisions with the vortex body, and finally are incorporated into the vortex body via re-reconnection (T = $60-70\Omega_i^{-1}$). Thus, the VIR process is composed of the island formation and incorporation and the associated two-stage reconnection process. Hence, in order to comprehensively understand the VIR process, it is important to reveal not only the first reconnection process discussed in section 3.2, but also the second re-reconnection process.

[19] The blue solid (dashed) line in Figure 7b shows time variation of the reconnected flux at the X point on the left side of island 3 (island 4) in Figure 7a. Here each value is obtained from the vector potential at the outer edge of each island. The absolute value of the negative peak of each line corresponds to the peak reconnection
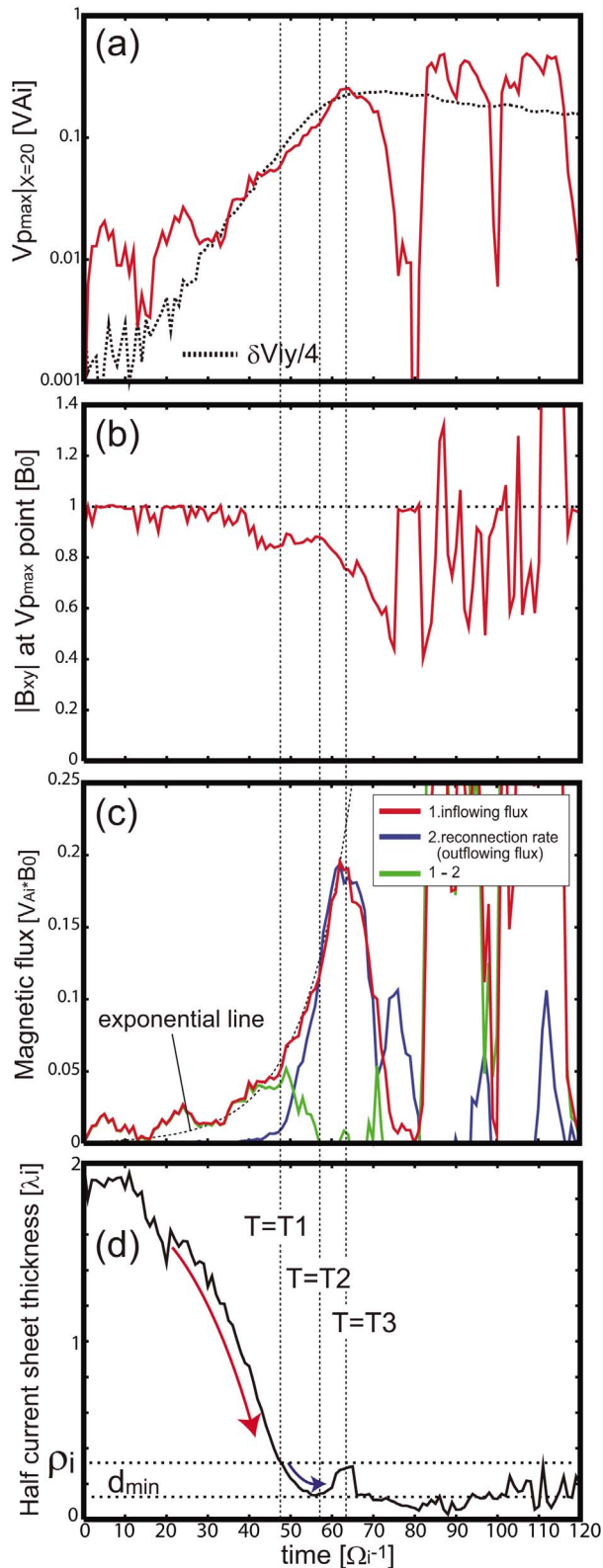
Figure 5. (a) The maximum ion flow speed V_{pmax} perpendicular to the magnetic field lines on $X = 20\lambda_i$ and (b) in-plane magnetic field intensity $|B_{XY}|$ at the maximum inflow (V_{pmax}) point as a function of time in the $D_0 = 2.0\lambda_i$ and $M_A = 4.375$ case. (c) Red line shows the magnetic flux flowing into X1 point (marked in Figure 4a), which is obtained by $|V_{pmax}|$ (Figure 5a) times $|B_{XY}|$ (Figure 5b). Blue and green lines in Figure 5c show the reconnection rate (same as Figure 3d), corresponding to the outflowing flux, and the difference between the inflowing and outflowing fluxes, respectively. (d) The half thickness of the compressed current sheet (same as Figure 3b). T1, T2, and T3 are the same as those in Figure 3.
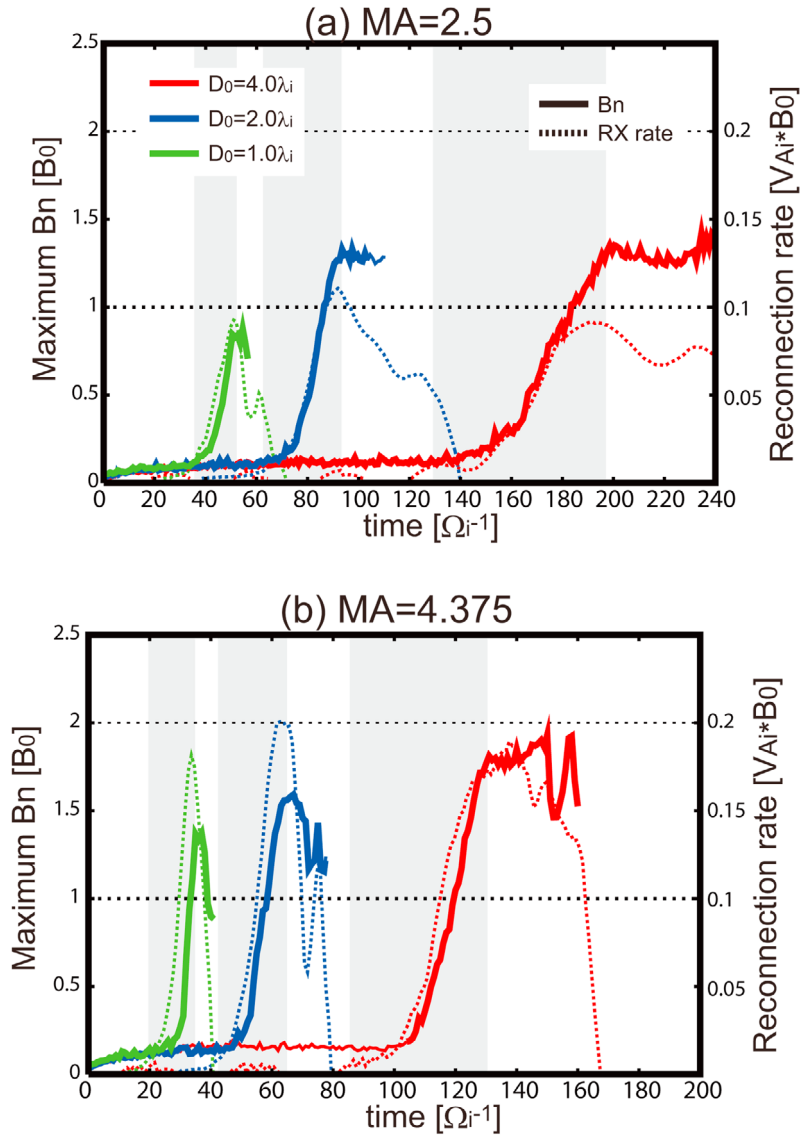
Figure 6. Reconnection rates (dashed) and maximum in-plane magnetic field intensities perpendicular to the current sheet (solid) as a function of time for $D_0 = 1\lambda_i$, $2\lambda_i$ and $4\lambda_i$ cases. Shown are the (a) $M_A = 2.5$ and (b) $M_A = 4.375$ cases.

rate at the re-reconnection point between each island and the vortex body. We see that the peak reconnection rates are both about $0.55 V_{Ai} \cdot B_0$, which is nearly three times the peak rate of the first reconnection induced at the compressed current sheet. These high reconnection rates can be regarded as resulting from the strong vortex flow and associated high-speed collisions of the islands. Indeed, we see that the peak reconnection rates both lie on the line of $0.59\ \delta V_{iY} \cdot B_0$ (black dashed curve in Figure 7b), that is, they are controlled by δV_{iY}. This result means that the rate of the second re-reconnection as well as the first reconnection is controlled by the vortex flow. In summary, both the multiple island formation and incorporation processes are controlled by the vortex flow, and therefore the associated two-stage reconnection process is of driven-type.

3.4. Generality of the Multiple Island Formation

[20] Next, we investigate the generality of the multiple island formation process by comparing the length of the current sheet with that of the islands, which is controlled by the current sheet thickness. Figure 8 shows the minimum thickness of the compressed current sheet d_{min} for various sets of (D_0, M_A) as a function of V_0/D_0, which is almost equivalent to the KHI growth rate γ_{KH}. We see that d_{min} decreases with increasing γ_{KH}. This can be explained using the $D_0 = 2.0\lambda_i$ and $M_A = 4.375$ case as follows: the growth rate γ_{inflow} of the inflowing magnetic flux f_{inflow} to the first reconnection region is basically constant since γ_{inflow} is roughly equal to γ_{KH}, as shown in section 3.2. On the other hand, the growth rate $\gamma_{outflow}$ of the outflowing flux $f_{outflow}$ basically depends on the current sheet thickness, since the reconnection occurs more rapidly as the current sheet thins.
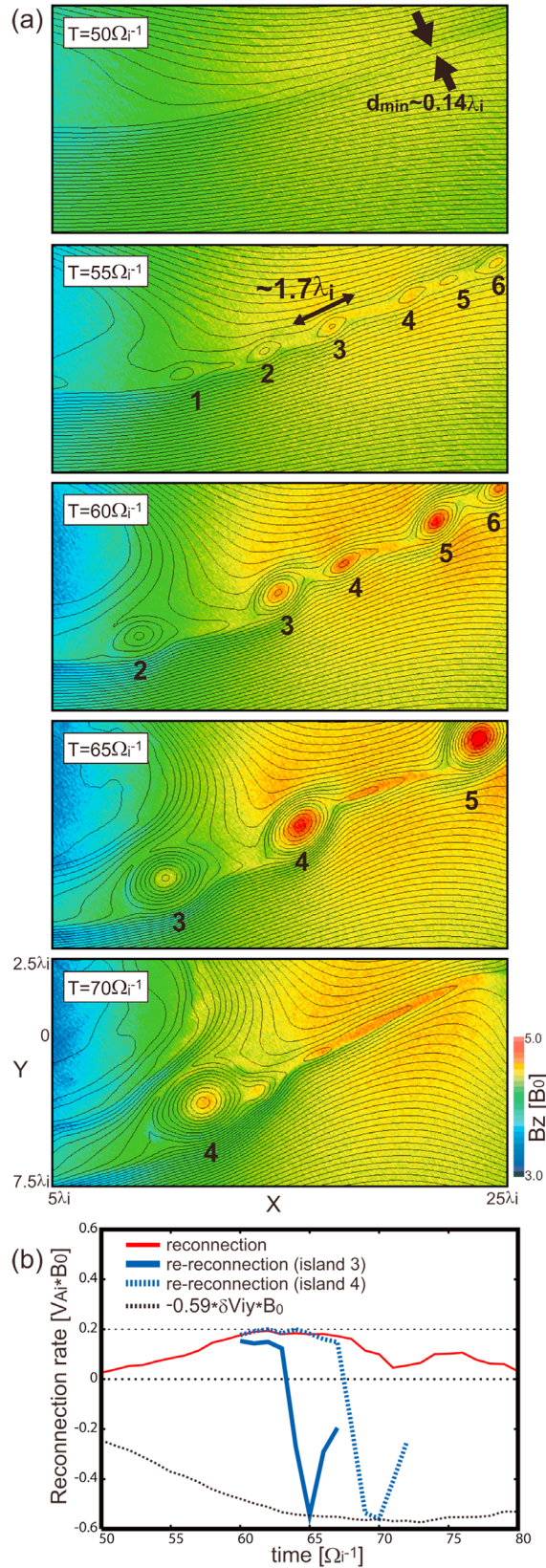
In the initial stage of the KHI growth, since $\gamma_{\mathrm{inflow}} \gg \gamma_{\mathrm{outflow}}$, the difference between f_{inflow} and f_{outflow} exponentially increases (black dotted line in Figure 5c), so that the current sheet thinning also exponentially progresses to sustain the excess inflowing flux (T $\ll$ T1 in Figure 5). When the current sheet thickness reaches ρ_i (T = T1 in Figure 5), $\gamma_{\mathrm{outflow}}$ rapidly increases and instantly exceeds γ_{inflow}. Then, f_{outflow} begins to approach f_{inflow}, and at the same time the current sheet thinning begins to be suppressed. When f_{outflow} eventually reaches f_{inflow}, the current sheet thinning stops (T = T2 in Figure 5). This indicates that γ_{inflow} ($\sim\gamma_{KH}$) in relation to $\gamma_{\mathrm{outflow}}$ controls and suppresses the current sheet thinning. In other words, if γ_{KH} is larger so that γ_{inflow} becomes larger, the current sheet needs to become thinner before the thinning stops; $d_{\min}$ tends to decrease with increasing γ_{KH}. When γ_{KH} is extremely large ($V_0/D_0 >$ 1.5), however, $d_{\min}$ approximates to a constant value $d_{\min} \sim \lambda_e/2$ regardless of γ_{KH}, where λ_e is the electron inertial length. This is because the lower limit of the current sheet thickness is determined by λ_e.
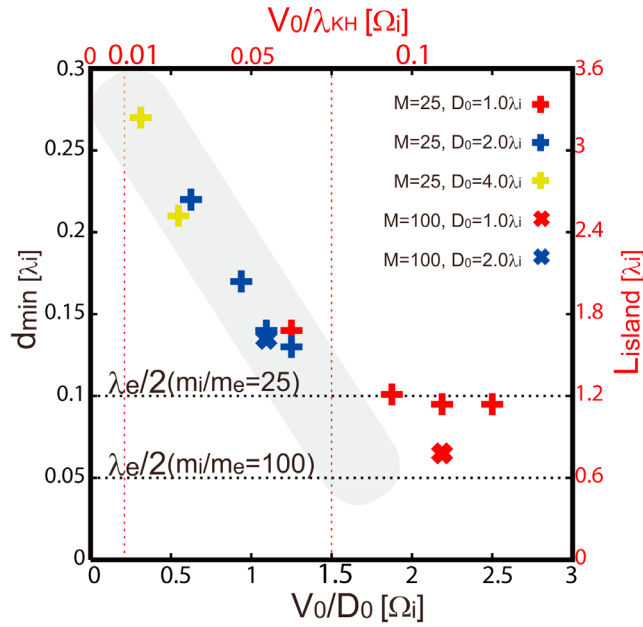
[21] The length of the compressed current sheet L_{cs} depends on the size of the vortex as $L_{cs} \sim \lambda_{KH}/4 \sim 5D_0$, whereas the typical length of multiple islands L_{island} depends on the current sheet thickness as $L_{\mathrm{island}} \sim 12 d_{\min}$. Since more than one magnetic island can be formed in the compressed current sheet when $L_{cs} > L_{\mathrm{island}}$, the condition for the multiple island formation would be $12 d_{\min} < 5D_0$, that is, $d_{\min}/D_0 < 0.4$ (Figure 9a). Figure 9b shows $d_{\min}$ normalized by D_0 as a function of M_A for the same runs as Figure 8. Since as mentioned above, $d_{\min}$ increases with decreasing V_0/D_0, $d_{\min}/D_0$ tends to increase as $M_A = V_0/V_{Ai}$ decreases when D_0 is fixed. In addition, we found that $d_{\min}/D_0$ tends to increase as D_0 decreases when V_0 is fixed. However, even in the smallest set of (D_0, M_A) ($D_0 = \lambda_i$ and $M_A = 2.5$ case), $d_{\min}/D_0$ is less than 0.4. This means that in MHD-scale situations ($D_0 \geq \lambda_i$), multiple islands could always appear in the compressed current sheet. Indeed, all simulations in this study show that more than one magnetic island, whose initial lengths are always about $12 d_{\min}$, are formed in the compressed current sheet (partially shown in Figure 10). In addition, all these islands move toward, and incorporate with, the vortex body (not shown). Thus, it can be concluded that the formation and incorporation of multiple islands is universal in the VIR process.

3.5. Magnetic Structure of the Multiple Islands

[22] It is also noteworthy that in-plane magnetic field lines tend to be strongly piled up within the magnetic islands formed through the VIR, as seen in Figure 10. Solid lines in Figure 6 show maximum intensities of the in-plane mag-

Figure 7. (a) Time series of the zoom-in view of the region marked by the black box in Figure 2. Color contours show the out-of-plane magnetic field component (B_Z). Magnetic islands formed in the compressed current sheet are numbered from left to right. (b) The blue solid (dashed) line shows time variation of the reconnected flux at the X point on the left side of island 3 (island 4) in Figure 7a. The red line shows the reconnection rate at the first reconnection site. The black dashed curve shows a line of $-0.59 \, \delta V_{iY} \cdot B_0$.
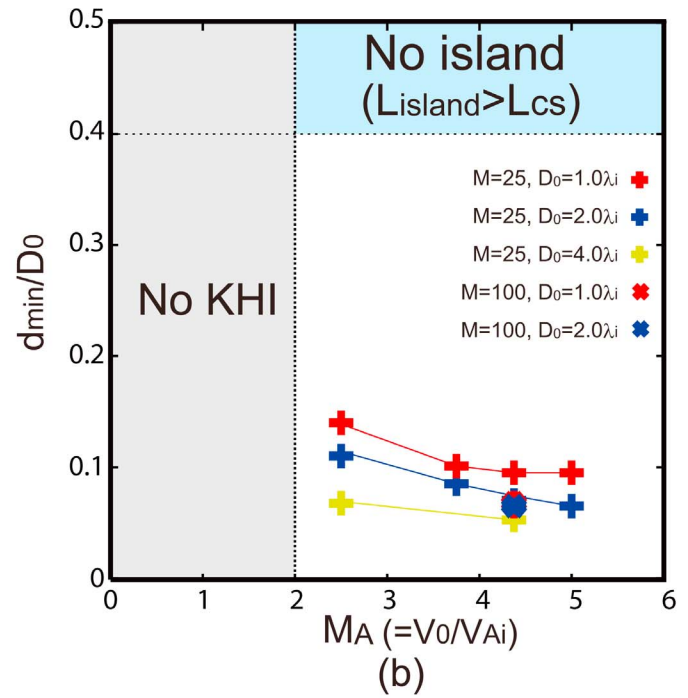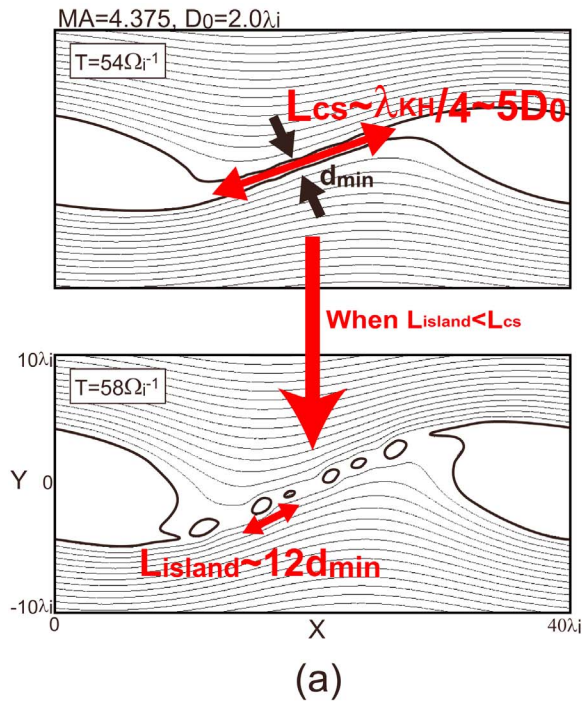
Figure 8. Minimum half thickness of the compressed current sheet d_{min} for various cases as a function of V_0/D_0, that is almost equivalent to the growth rate of the KHI. Note that d_{min} corresponds to $1/12$ times the length L_{island} of the magnetic island formed in the compressed current sheet, and V_0/D_0 corresponds to 20 times V_0/λ_{KH} since λ_{KH} is set to be $20D_0$.

netic field component normal to the current sheet B_{nmax} and the reconnection rate as a function of time for $D_0 = 1\lambda_i$, $2\lambda_i$ and $4\lambda_i$ cases. B_{nmax} is found to occur at the most piled-up region. In all cases except for the $D_0 = 1.0\lambda_i$ and $M_A = 2.5$ case, the peak values of the most piled-up field intensity are stronger than the background value (B_0). Interestingly, in the $D_0 = 4.0\lambda_i$ and, $M_A = 4.375$ case, the piled-up field intensity is about twice the background value. These peak values tend to be stronger as D_0 (the size of the vortex) or M_A (the shear flow intensity) increases. This can be explained as follows: during the period $\Delta T_{pile-up}$ when the piled-up field intensity is increasing (shaded periods in Figure 6), the reconnection rate R_{RX} also increases, that is, the magnetic flux continues to be stored within the islands. Since $\Delta T_{pile-up}$ increases as the size of the vortex ($\propto D_0$) increases and since R_{RX} increases as M_A increases, stronger magnetic field pileup occurs for larger D_0 or M_A. Such a characteristic in-plane magnetic structure could be confirmed by in situ observations as evidence for the occurrence of the VIR at the Earth's magnetopause (as discussed further in section 5.2).

[23] During the period $\Delta T_{pile-up}$, the out-of-plane magnetic field (B_Z) within the islands also increases. Color contours in Figure 7a show a time series of B_Z in the $D_0 = 2.0\lambda_i$ and, $M_A = 4.375$ case. We see that B_Z is enhanced inside the piled-up region of the islands, that is, at the core part of the islands. This is because the islands are contracted by the in-plane magnetic tension exerted by the piled-up field. The core field (B_Z) enhancement becomes stronger with increasing the piled-up field intensity, although the enhancement is eventually suppressed as the piled-up field

Figure 9. (a) Sketch of the formation process of multiple magnetic islands in the compressed current sheet. When $12d_{min} < 5D_0$ ($d_{min}/D_0 < \sim 0.4$), $L_{island} < L_{cs}$, and thus more than one magnetic island can be formed. (b) Minimum half thickness of the compressed current sheet d_{min} normalized by D_0 for various cases as a function of M_A.
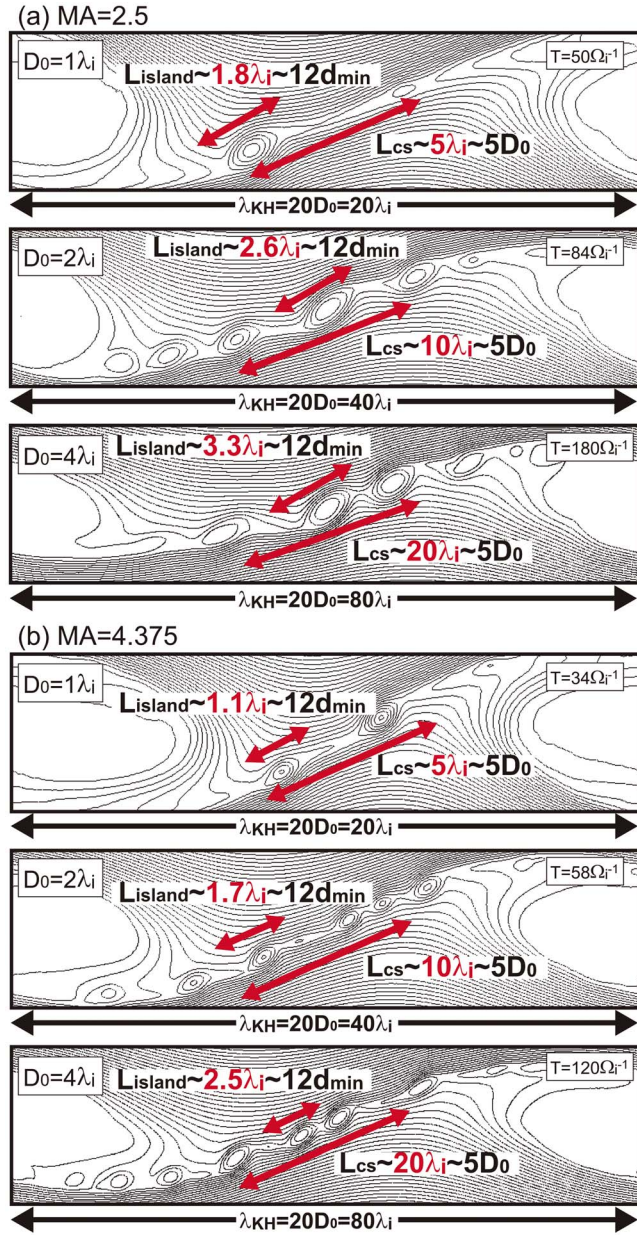
Figure 10. In-plane magnetic field lines at the initial stage of the VIR in the compressed current sheet for $D_0 = 1\lambda_i$, $2\lambda_i$ and $4\lambda_i$ cases. Shown are the (a) $M_A = 2.5$ and (b) $M_A = 4.375$ cases. In all cases, more than one island, whose initial lengths are always about $12d_{min}$, are formed.

is removed by the re-reconnection (see island 3 or 4 in Figure 7a). Note, however, that the maximum core field enhancement is only about 18 percent of the background B_Z intensity. In addition, all simulations in this study show that the maximum core field enhancements are always less than 20 percent of the background intensity (not shown). This can be explained as follow: since B_Z is dominant in this study ($B_{Z0} \sim 4B_{X0}$), the in-plane magnetic tension can only slightly contract the islands to balance the pressure from the strong out-of-plane magnetic field. Thus, the core field within the VIR-associated islands is not expected to show a

significant enhancement in the presence of strong guiding magnetic field.

### 3.6. Comparison With Two-Fluid Simulations

[24] We further compare the particle simulation results in the $D_0 = 2.0\lambda_i$ and $M_A = 4.375$ case with those of a two-fluid (TF) simulation using the same initial settings regarding m_i/m_e, the spatial resolution, and the magnetic field, velocity, density and temperature profiles (the results are shown in Figures 3 and 11). In the TF system, since the electron inertial term can break the frozen-in condition, reconnection can occur spontaneously with no anomalous resistivity. The TF code is explained in detail by *Nakamura et al.* [2008]. First, we found that the linear growth rate of the KHI in the particle case is slightly lower than in the TF case (Figure 3a). This is due to the ion gyromotion which slightly broadens the shear layer even when $D_0 > \rho_i$. Such a slight decrease of the KHI growth rate was seen in past particle simulations for $D_0 = 2\lambda_i$ cases [see *Nakamura et al.*, 2010, Figure 7].

[25] Regarding the VIR, we found a significant difference between the two kinds of simulations. In the particle case, reconnection visibly grows after $T \sim 48\Omega_i^{-1}$ (T1), whereas in the TF case, the VIR visibly grow only after $T \sim 56\Omega_i^{-1}$ (Figure 3d). This delay of the VIR generation in the TF case is attributed to the lack of the ion kinetic effects: in the TF case, only electron inertial effects can contribute to the growth of reconnection. In the particle case, on the other hand, since the gyroradius of thermal ions ($\sim 0.26\lambda_i$) is larger than the minimum current sheet thickness ($\sim 0.14\lambda_i$), the ion meandering motion across the current sheet can assist the growth of reconnection [e.g., *Pei et al.*, 2001b].

[26] The delay of the VIR in the TF case allows an enhancement of the plasma pressure at the center of the
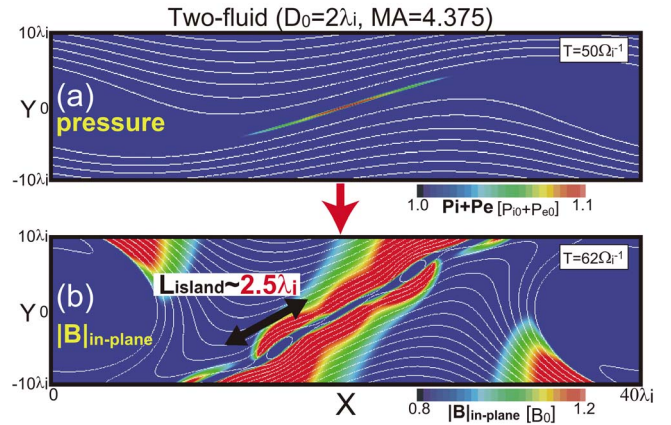
Figure 11. Two-fluid simulation result in the $D_0 = 2.0\lambda_i$ and $M_A = 4.375$ case. (a) Plasma pressure ($P_i + P_e$) at $T = 50\Omega_i^{-1}$ with in-plane magnetic field lines overlaid. The range of the color contour is set to present only values in excess of the maximum value at $T = 0$. (b) In-plane magnetic field intensity at $T = 62\Omega_i^{-1}$ with in-plane magnetic field lines overlaid. The typical length of magnetic islands formed in the compressed current sheet is about $2.5\lambda_i$, which is about 1.5 times larger than in the particle case.
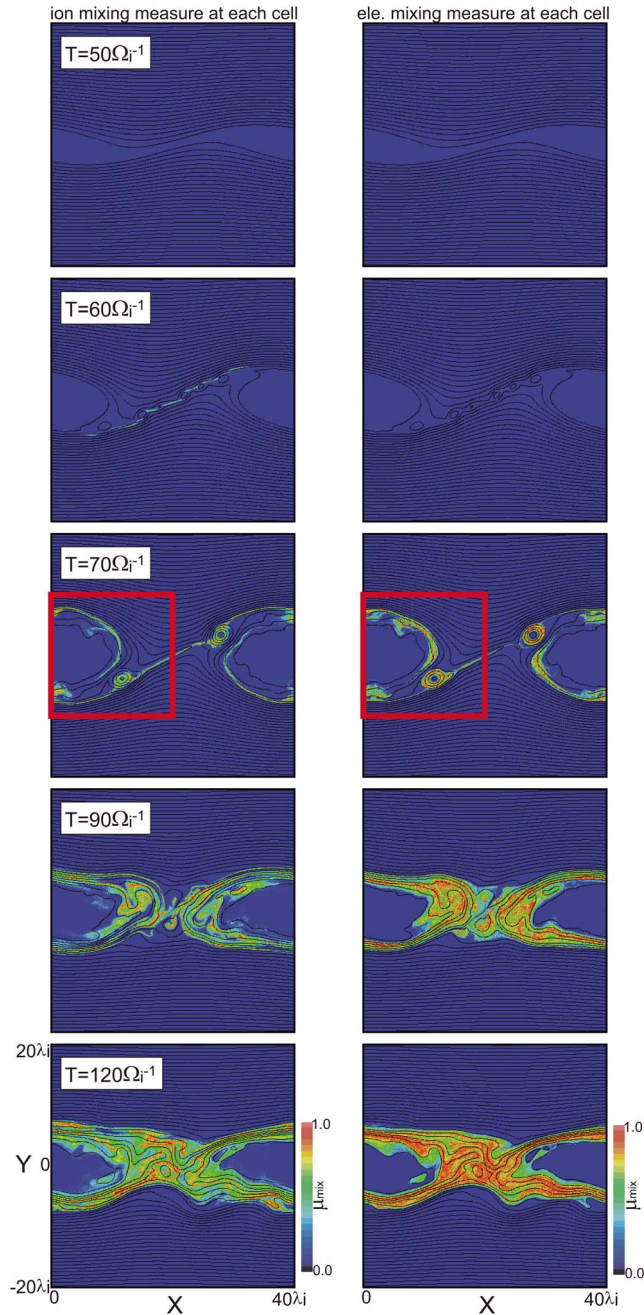
Figure 12. Time series of the mixing measure in each cell for particles which initially exist in $Y > D_0$ and $Y < -D_0$ in the $D_0 = 2.0\lambda_i$ and $M_A = 4.375$ case (see text for definition of the mixing measure). Shown are the (left) ion and (right) electron mixing measures.

compressed current sheet (Figure 11a). Such a clear pressure enhancement does not appear in the particle case, since the enhancement tends to be relaxed by reconnection (not shown). This pressure enhancement in the TF case tends to prevent the current sheet thinning (see the period around T = 50–65Ω_i^{-1} in Figure 3b). Consequently, the typical length of magnetic islands formed in the compressed current sheet in the TF case is larger than in the particle case (Figure 11b).

Furthermore, the pressure enhancement is also accompanied with the accumulation of excess magnetic flux at the edge of the current sheet (Figure 11b). The accumulated in-plane magnetic field leads to the larger reconnection rate (Figure 3d), since the reconnection rate depends on the in-plane field intensity in the inflow region. Thus, the ion kinetic effects must be taken into account to exactly understand physics of the VIR and the associated multiple island formation when the minimum half thickness of the compressed current sheet d_{min} is smaller than the ion gyroradius ρ_i. As shown in Figure 8, since d_{min} tends to increase with decreasing the KHI growth rate V_0/λ_{KH}, whether the ion kinetic effects shown in this section can appear or not is determined by ρ_i and V_0/λ_{KH}. In our simulation settings, since $\rho_i \sim 0.26$, the ion kinetic effects turn on when V_0/λ_{KH} exceeds about 0.01.

4. Kinetic Roles of the Vortex-Induced Reconnection

4.1. Plasma Mixing Process

[27] Magnetic reconnection has been considered to play a key role in mixing plasmas in real space along reconnected field lines. In this section, we investigate the efficiency of the plasma mixing caused by the VIR. Figure 12 shows a time series of the mixing measure in each cell in the $D_0 = 2.0\lambda_i$ and $M_A = 4.375$ case (the same case as Figure 2). The mixing measure, defined as the smaller one of $2N_1/(N_1 + N_2)$ and $2N_2/(N_1 + N_2)$, is a measure of the abundance of particles originated in the other side of the shear layer. Here N_1 and N_2 are the number of particles in cell which initially exist at $Y > D_0$ (upper region of the shear layer) and $Y < -D_0$ (lower region of the shear layer), respectively. Figure 12 (left) (Figure 12, right) shows the ion (electron) mixing measures. At first, both ions and electrons begin to mix around the multiple X points in the compressed current sheet (T~60Ω_i^{-1}). Then, the areas of mixed ions and electrons broaden along reconnected field lines by thermal motion of ions and electrons, respectively. Finally, a substantial region within the vortex becomes filled with the well-mixed ions and electrons (T~120Ω_i^{-1}). Solid lines in Figure 13a show the total number of mixed ion (red) and electron (blue) cells as a function of time, normalized by the total number of cells N_{total} in the region $|Y| < 20\lambda_i$ and $0 < X < 40\lambda_i$. A mixed cell is defined as the cell in which the mixing measure $\mu_{mix} > 0.25$. We see that the mixed area for both ions and electrons broadens from T~60Ω_i^{-1}, and the broadening of the mixed ion (electron) area is saturated at T~140Ω_i^{-1} (T~120Ω_i^{-1}).

[28] It is notable here that the areas of both mixed ions and electrons broaden most efficiently during the interval when the multiple X line reconnection continues (shaded period in Figure 13a). Figure 14 shows a time series of the zoom-in view of the region marked by red boxes in Figure 12 for this period. The mixed plasma areas begin to broaden from the multiple X points (T~62Ω_i^{-1}), and then the multiple islands become filled with the mixed plasmas (T~66Ω_i^{-1}). Subsequently, the multiple islands with well-mixed plasmas are incorporated into the vortex body, and consequently the plasma mixing rapidly progresses within the vortex (T~70–74Ω_i^{-1}). These results clearly imply that the multiple island (X line) formation results in the fast broadening of the mixed

(a)

(b)
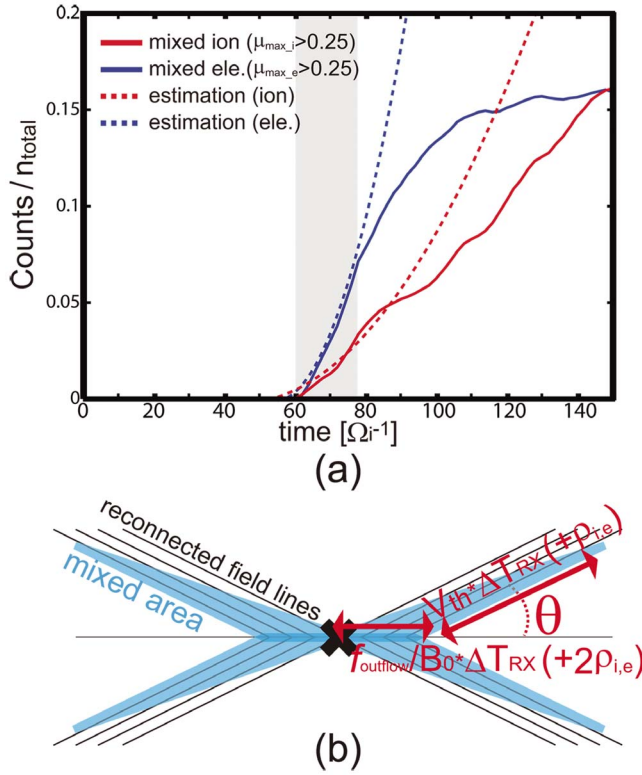
Figure 13. (a) Solid lines show the total number of mixed ion (red) and electron (blue) cells normalized by the total number of cells in the region $|Y| < 20\lambda_i$ and $0 < X < 40\lambda_i$ as a function of time in the $D_0 = 2.0\lambda_i$ and $M_A = 4.375$ case. A mixed cell is defined as the cell in which the mixing measure $\mu_{\mathrm{mix}} > 0.25$. Dashed lines show estimates of the ion (red) and electron (blue) mixed areas (see text for details). (b) Sketch of the mixed plasma area around a perfectly X-shaped X line with a constant reconnection rate.

areas. This mixing can be quantified as follows: assuming a perfectly X-shaped X line with a constant reconnection rate (outflowing magnetic flux) as illustrated in Figure 13b, the mixed area around an X line at a given time can be described as $4 \cdot (R_{RX}/B_0 \cdot \Delta T_{RX}) \cdot (V_{th} \cdot \Delta T_{RX} \cdot B_0/\sqrt{B_0^2 + B_z^2})/2 \cdot \sin\theta$. Here θ is the angle between the neutral sheet and reconnected field lines, and ΔT_{RX} is the time from the start of reconnection at the X line. Note that $B_0/\sqrt{B_0^2 + B_Z^2}$ is a factor regarding the actual length of the field lines, which is about $\sqrt{B_0^2 + B_Z^2}/B_0$ times longer than the length viewed in the two-dimensional simulation plane. Since the total mixed area increases with the number of X points N_X, the time evolution of the total mixed area can be described as

$$N_{estimation}/N_{total} \sim N_X \cdot 4 \cdot \left(R_{RX}/B_0 \cdot \Delta T_{RX} + 2\rho_{i,e}\right)$$
$$\cdot \left(V_{th} \cdot \Delta T_{RX} \cdot B_0/\sqrt{B_0^2 + B_z^2} + \rho_{i,e}\right)/2$$
$$\cdot \sin\theta/(40\lambda_i)^2, \tag{1}$$

where we add the terms using $\rho_{i,e}$, representing a rough estimate of mixing regions produced by the particle gyromotion whose guiding centers exist at the edge of the mixing

regions. Dashed lines in Figure 13a show the mixed ion (red) and electron (blue) areas estimated from equation (1), where we assume $R_{RX} = 0.15$ (the average value during the shaded period in Figure 13a), and $\theta = 30$ degrees. We see that these estimates are roughly consistent with the simulation results during the shaded period. After the shaded period (T > $78\Omega_i^{-1}$), since the number of the reconnected field lines does not increase (that is, $R_{RX}/B_0 \cdot \Delta T_{RX}$ does not increase), the broadening of the mixed ion area is suppressed. Thus, it is concluded that the efficiency of the plasma mixing basically increases with increasing N_X, R_{RX}, or V_{th}. Since as shown in section 3, the VIR tends to involve multiple X lines with a high reconnection rate ($N_X \geq 1$, and $R_{RX} > 0.1$), it can also be concluded that the plasma mixing caused by the VIR is more efficient than spontaneous reconnection with single X line ($N_X = 1$, and $R_{RX} \leq 0.1$).

4.2. The Electron Acceleration Process

[29] Reconnection has also been considered to play a key role in producing high-energy particles in space [e.g.,
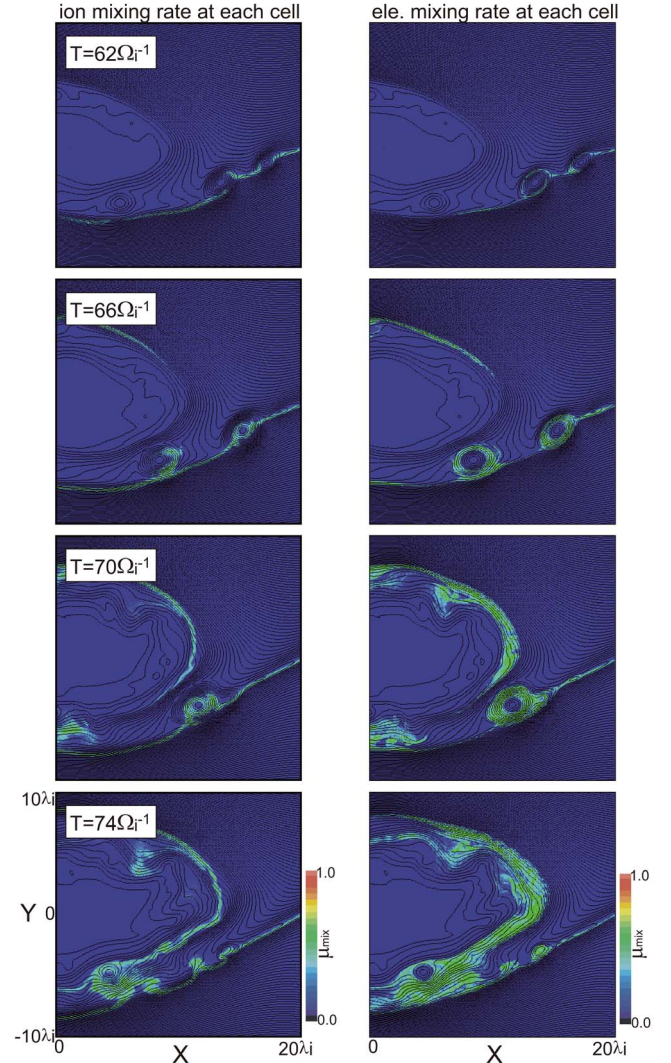
Figure 14. Time series of the zoom-in view of the region marked by the red box in Figure 12.

Hoshino et al., 2001; *Hoshino*, 2005; *Pritchett and Coroniti*, 2004; *Drake et al.*, 2006]. In this section, we investigate how the VIR accelerate electrons. Figure 15b shows color contours of $E_Z + (\mathbf{V_e} \times \mathbf{B})_Z$, which represents the reconnection
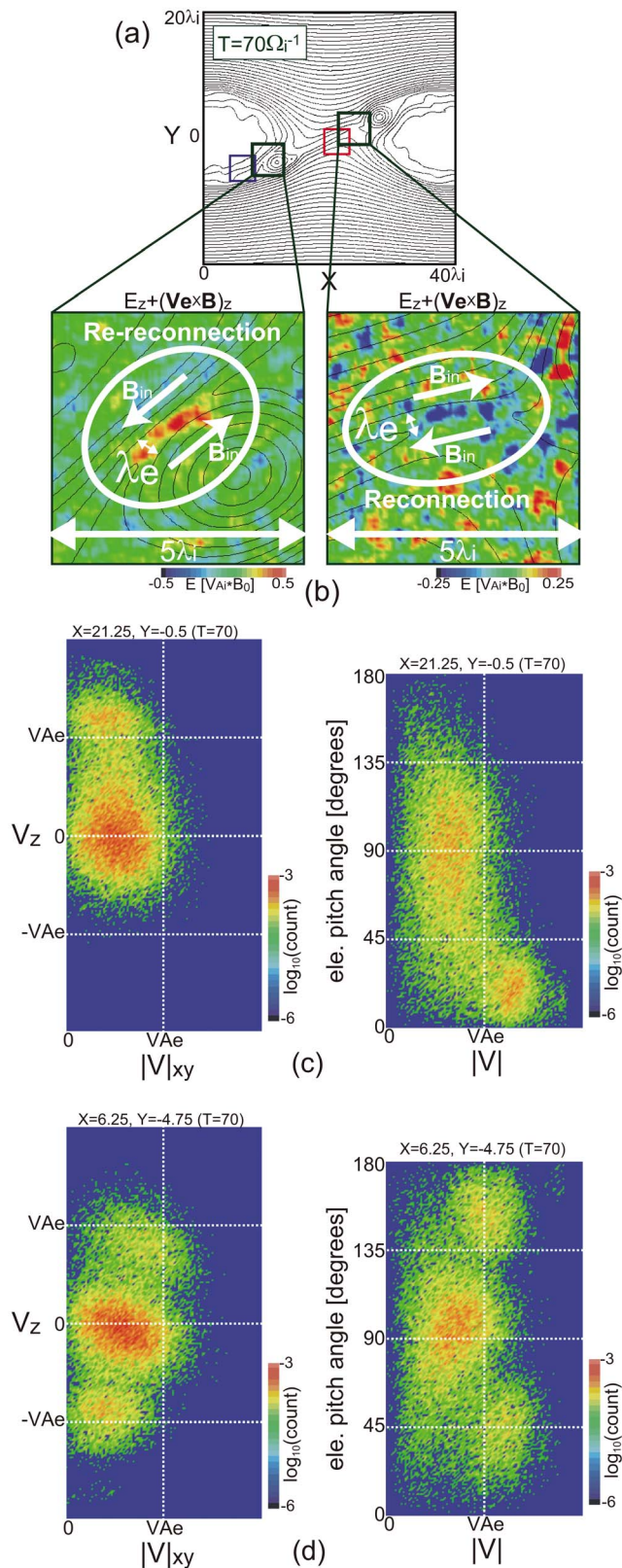
electric field at points of the first reconnection (Figure 15, right) and the second re-reconnection (Figure 15, left) in the $D_0 = 2.0\lambda_i$ and $M_A = 4.375$ case. At the first reconnection point, a negative reconnection electric field appears. The intensity of the reconnection electric field is about $0.2V_{Ai} \cdot B_0$, which is equivalent to the reconnection rate at this X point. At the second re-reconnection region, in contrast, a positive reconnection electric field appears, since the in-plane magnetic field direction across the re-reconnection region is opposite from that across the first reconnection region. The intensity of the re-reconnection electric field is about $0.5V_{Ai} \cdot B_0$, which is equivalent to the reconnection rate at this X point. The thickness and length of the region with the reconnection electric field are about λ_e and $5\lambda_e$, respectively, for both types of reconnection.

[30] Figure 15c show velocity distribution functions (Figure 15c, left) and pitch angle distributions (Figure 15c, right) of electrons in the downstream region of the reconnection point, surrounded by the red box in Figure 15a. We see that there are two populations of electrons: background thermal electrons and nonthermal electrons accelerated in the $+Z$ direction by the negative reconnection electric field. Note that since the $+Z$ component of the magnetic field is dominant in this study ($B_{Z0} \sim 4B_{X0}$), the electron acceleration (in the $+Z$ direction) occurs almost along the magnetic field direction.

[31] In the downstream region of the re-reconnection point (Figure 15d), on the other hand, there are three populations of electrons: background thermal electrons, nonthermal electrons accelerated in the $+Z$ direction (almost along the parallel direction), and nonthermal electrons accelerated in the $-Z$ direction (almost along the antiparallel direction). The nonthermal, antiparallel population is composed of electrons accelerated by the positive electric field of re-reconnection. The nonthermal, parallel population is composed of electrons which have been accelerated at the first reconnection region in the compressed current sheet and are carried into the vortex body along with the multiple islands. It means that the nonthermal, parallel and antiparallel populations are mixed within the vortex through the multiple island incorporation process.

[32] While the intensity of the reconnection electric field is more than twice higher for the second re-reconnection than for the first reconnection (Figure 15b), our simulation results show that the change in the electron speed ΔV_e in both reconnection processes is always about the electron Alfvén speed V_{Ae} (Figures 15c and 15d). This result can be explained by simple acceleration by the reconnection electric field as follows: in our simulations, since the out-of-plane magnetic field and associated convective electric field are dominant, when seen in the plane of the simulation, electrons basically move along the vortex flow. Thus, the

Figure 15. (a) In-plane magnetic field lines at T = $70\Omega_i^{-1}$ in the $D_0 = 2.0\lambda_i$ and $M_A = 4.375$ case. (b) Color contours of $E_Z + (\mathbf{V_e} \times \mathbf{B})_Z$ around (right) the reconnection point and (left) the re-reconnection point. (c, d) (left) Electron velocity distribution functions and (right) pitch angle distributions at T = $70\Omega_i^{-1}$ in the downstream region of reconnection (Figure 15c), marked by the red box in Figure 15a and in the downstream region of re-reconnection (Figure 15d), marked by the blue box in Figure 15a.
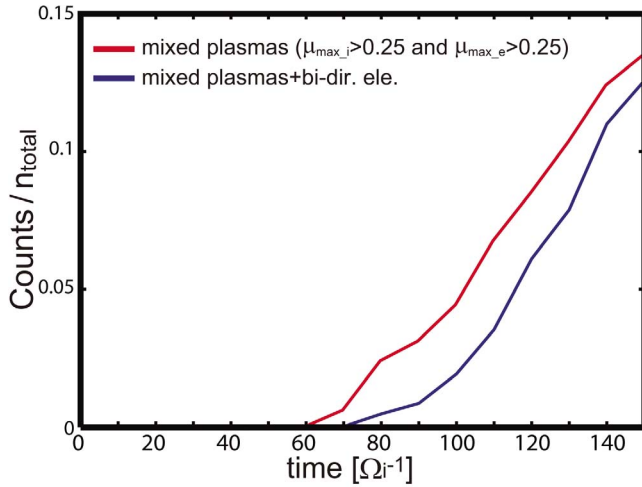
Figure 16. The total number of (red) cells with both mixed ions and mixed electrons, and (blue) cells where the mixed plasmas and bidirectionally accelerated electrons coexist, normalized by the total number of cells in the region $|Y| < 20\lambda_i$ and $0 < X < 40\lambda_i$ as a function of time in the $D_0 = 2.0\lambda_i$ and $M_A = 4.375$ case.

acceleration time period, the time taken by electrons to pass through the region with the reconnection electric field, can be roughly estimated as $\Delta T_{acceleration} \sim L_e/V_{convect} \propto \lambda_e/V_{inflow}$. Here L_e is the size of the electron diffusion region perpendicular to the in-plane magnetic field lines, which can be scaled by the electron inertial length, and $V_{convect}$ is the electron convection speed in the diffusion region, which can be represented by the reconnection inflow speed V_{inflow}. Hence, the speed change can be roughly estimated as

$$\Delta V_e \sim \frac{e}{m_e} \cdot E_{RX} \cdot \Delta T_{acceleration} \propto \frac{e}{m_e} \cdot V_{inflow} \cdot B_0 \cdot \lambda_e/V_{inflow} = V_{Ae},$$

(2)

where E_{RX} is the reconnection electric field. This estimation predicts that ΔV_e is controlled by V_{Ae} only, regardless of the reconnection inflow speed. This prediction agrees reasonably with the above simulation results. Note that ΔV_e ($\sim V_{Ae}$) in the VIR is close to that in the spontaneous reconnection without [e.g., *Hoshino et al.*, 2001] and with a guiding magnetic field [*Pritchett and Coroniti*, 2004]. Also note that in this study, since the ratio between the light speed c and V_{Ae} is set to be $c/V_{Ae}(=\omega_{pe}/\Omega_e) = 2$, ΔV_e in equation (2) is about 0.5c. In addition, the thermal speed of electrons is set to be 0.17c. The Lorentz factors for most accelerated electrons are therefore small enough not to significantly change equation (2) described in a nonrelativistic form, although a fraction of electrons is accelerated to a relativistic energy. Relativistic effects need to be considered seriously in smaller ω_{pe}/Ω_e cases. Around the Earth's magnetopause, however, since ω_{pe}/Ω_e is known to be always larger than 2, the relativistic effects would be negligible.

[33] In addition to the above simple acceleration mechanism in the reconnection region, it has been proposed that electrons can be accelerated even outside the reconnection region [e.g., *Hoshino et al.*, 2001; *Hoshino*, 2005; *Drake*

et al., 2006]. *Hoshino* [2005] has shown that in the driven reconnection system, electrons can be strongly accelerated near the reconnection region due to a surfing acceleration mechanism; just outside the reconnection region, some electrons are trapped by the electrostatic potential associated with the Hall current, and can efficiently gain energies therein. *Hoshino et al.* [2001] also revealed that the electrons accelerated in or near the reconnection region can be secondarily accelerated while the electrons are trapped in the region of reconnected field pileup. Furthermore, it has recently been proposed that electrons can also be accelerated within secondary multiple islands during magnetic reconnection due to the contraction of the islands [*Drake et al.*, 2006]. In this study, however, these types of acceleration outside the reconnection region cannot be observed. This is because in the VIR, electrons, moving along the dominant vortex flow, cannot be trapped by either the electrostatic potential or the piled-up field within the multiple mesoscale islands. In addition, the pressure from the dominant out-of-plane magnetic field prevents the multiple islands from contracting significantly (section 3.5).

4.3. Coexistence of Mixed Plasmas and Accelerated Electrons

[34] As shown in section 4.1, the second re-reconnection injects well-mixed ions and electrons, produced by the first reconnection and carried by the multiple islands, into the vortex. As shown in section 4.2, the second re-reconnection also mixes within the vortex electrons accelerated almost in the parallel direction by the first reconnection and those accelerated almost in the antiparallel direction by itself. These results indicate that a series of the first reconnection (multiple island formation) and second re-reconnection (multiple island incorporation) processes can produce a region within the vortex where the mixed plasmas and bidirectionally accelerated electrons coexist. Figure 16 shows, as a function of time, the total number of (red) cells with both mixed ions and electrons, and of (blue) cells with both the mixed plasmas and bidirectionally accelerated electrons, normalized by N_{total} in the region $|Y| < 20\lambda_i$ and $0 < X < 40\lambda_i$. Here a mixed cell is defined as the cell where the mixing measures for both ions and electrons exceed 0.25, and a cell with bidirectionally accelerated electrons is defined as the cell where the average $|V_Z|$ for electrons with $V_Z > 0$ and that for those with $V_Z < 0$ both exceed 1.1 times the electron thermal speed. We see that a majority of the mixed area is filled with the bidirectionally accelerated electrons. Especially in the stage of the highly rolled-up KH vortex ($T \sim 150\Omega_i^{-1}$), more than 90 percent of the mixing area is filled with these electrons. Thus, it can be concluded that the mixed plasmas and bidirectional electrons tend to coexist within the rolled-up vortex as a result of a series of the multiple island formation and incorporation processes.

5. Summary and Discussion

5.1. Summary

[35] We have performed 2.5-dimensional full particle simulations of the VIR, focusing on fundamental situations with no asymmetry across the initial velocity shear layer.

First, fundamental properties of the VIR revealed by this study are summarized as follows.

[36] 1. At first, the flow of the KH vortex strongly compresses the current sheet. The minimum thickness of the compressed current sheet decreases with increasing the KHI growth rate, and its lower limit is about the electron inertial length λ_e.

[37] 2. Subsequently, magnetic reconnection is induced generally at multiple points (that is, magnetic islands are formed) in the compressed current sheet.

[38] 3. These multiple mesoscale islands are carried toward the vortex body along the vortex flow and then are incorporated into the vortex body via re-reconnection.

[39] 4. Maximum rates of both the first reconnection and second re-reconnection generally exceed 0.1. In other words, both reconnection processes are of driven-type.

[40] 5. In-plane magnetic field lines are strongly piled up within the island. The most piled-up field intensity can often exceed the background value ($B_{nmax} > B_{in}$).

[41] Next, we investigated kinetic roles of the VIR, focusing particularly on the plasma mixing and electron acceleration processes. The results are summarized as follows.

[42] 1. The plasma mixing within the vortex occurs along reconnected field lines, and the mixing area basically broadens by the thermal motion of particles.

[43] 2. The mixed area broadens more rapidly with increasing the number of X points, the rate of the first reconnection, or the thermal speed of particles.

[44] 3. The second re-reconnection mixes, within the vortex, electrons accelerated in the direction parallel to the magnetic field by the first reconnection and those accelerated in the antiparallel direction by itself. These electrons are accelerated up to about the electron Alfvén speed V_{Ae}.

[45] 4. Consequently, mixed plasmas and bidirectionally accelerated electrons tend to coexist within the rolled-up vortex.

[46] Fortunately, since recent Cluster observation at the Earth's magnetopause has successfully confirmed direct evidence of the VIR [*Hasegawa et al.*, 2009], our simulation results can be compared with the in situ observation data, which is done in section 5.2. However, it must be noted that this is the first study of the VIR using particle simulations, and thus this fundamental study still leaves some issues, as discussed in section 5.3, that should be addressed in the future in order to make more detailed comparisons with actual situations.

5.2. Observations of the Vortex-Induced Reconnection
5.2.1. Magnetic Island Formation
[47] We have revealed in this study that the generation of magnetic islands with strong magnetic field pileup is a general feature of the VIR process. Interestingly, in the Cluster VIR event reported by *Hasegawa et al.* [2009], Cluster 4 (C4) observed a flux rope-like, bipolar B_N fluctuation when C3, separated from C4 by ~1000 km, detected direct evidence of the VIR while crossing a thin current sheet [see *Hasegawa et al.*, 2009, Figure 8]. Here B_N is the field component normal to the current sheet. From the duration of the B_N fluctuation (~5 s) and the in-plane ion flow speed $|V_L|$ along the current sheet (~100 km/s), the size of the observed flux rope (magnetic island) can

be roughly estimated as $L_{island} \sim 500$ km. This size is consistent with our simulation results: in the Cluster VIR event, since the velocity jump across the current sheet was comparable to the Alfvén speed on the magnetosheath side ($V_0 \sim V_{Ai}$), and the estimated KH wavelength exceeded 10^2 times λ_i on the magnetosheath side ($\lambda_{KH} > 10^2 \lambda_i$), V_0/λ_{KH} was less than $10^{-2} \Omega_i$. In this small V_0/λ_{KH} situation, the size of the magnetic island expected from Figure 8 is about $L_{island} \sim 3.5 \lambda_i \sim 350$ km.

[48] Furthermore, the amplitude of the B_N fluctuation was comparable to the background in-plane field (B_L) intensity, and the B_L intensity during the B_N fluctuation was about 30 percent above the background value. Thus, the piled-up in-plane field intensity within the observed island can be interpreted as exceeding the background in-plane field intensity. This result is also consistent with our simulations showing that even in the low M_A case, the piled-up field intensity tends to exceed the background intensity as long as λ_{KH} is larger than $40\lambda_i$ (see Figure 6). Since the observed wavelength exceeds $10^2 \lambda_i$, the piled-up field intensity within the observed island is expected to exceed the background value. Thus, from the viewpoint of both the size and in-plane magnetic structure of the magnetic island, the observed flux transfer event-like B_N fluctuation can be interpreted as a signature of a moving flux rope (magnetic island) formed by the VIR. As shown in Figure 8, since the size of a magnetic island resulting from the VIR exceeds λ_i unless the KHI growth rate is extremely large ($V_0/D_0 = 20V_0/\lambda_{KH} > 1.5$), the VIR-associated island can basically be resolved by present-day observations. Direct observation of such a magnetic island on KH waves could be new observational evidence for the occurrence of the VIR.

5.2.2. Earth's LLBL Formation
[49] In the Earth's LLBL, the mixed ion region is almost always accompanied with field-aligned, bidirectional electrons [e.g., *Fujimoto et al.*, 1998; *Hasegawa et al.*, 2003]. Since the typical energy of these bidirectional electrons is higher than that of magnetosheath electrons, the LLBL formation would be accompanied by field-aligned, bidirectional acceleration of electrons. The KH vortex is believed to be an important ingredient for the LLBL formation under northward IMF conditions [e.g., *Sckopke et al.*, 1981; *Nakamura et al.*, 2006, 2008]. *Nakamura et al.* [2008] have suggested, based on linear analysis, that the growth of the KH vortex tends to involve reconnection. Furthermore, particle simulations of this study revealed that the VIR can produce both mixed plasmas and bidirectionally accelerated electrons within the rolled-up KH vortex. In addition, *Hasegawa et al.* [2006] showed that rolled-up vortices are mostly observed at the tail flank magnetopause when the IMF direction is northward. These results strongly suggest that the VIR could partly contribute to the formation of the tail flank LLBL under northward IMF conditions.

[50] Since the above Cluster VIR event [*Hasegawa et al.*, 2009] was accompanied with the magnetic island formation, it can be taken as representing the initial stage of the VIR shown in Figure 10. Interestingly, *Hasegawa et al.* [2009] have also reported that electrons accelerated along magnetic field lines were present around the VIR region. These electrons had a clear phase space density peak at about the electron Alfvén speed V_{Ae} in the magnetosheath. Since the speed of the accelerated electrons roughly agrees

with the value expected in the initial stage of the VIR (see Figures 15c and 15d), this observation supports that the VIR can actually produce not only mixed plasmas but also field-aligned electrons, that is, the VIR can actually form part of the LLBL. Thus, such a direct observation of beam-like accelerated electrons around the VIR region could be new observational evidence for the partial LLBL formation resulting from the VIR. While detailed velocity distributions to resolve the electron-scale reconnection region cannot be obtained by present-day observations, this Cluster observation presents the possibility that high time resolution observations of the next generation could resolve the VIR region and quantify the role of the VIR in the tail flank LLBL formation.

5.3. Some Remarks on Future Work

[51] While the symmetry across the initial velocity shear layer is assumed in this fundamental study, actual velocity boundaries such as the Earth's magnetopause often have moderate asymmetries of density, temperature and magnetic field structure. When these actual asymmetries are taken into account, the reconnection rate and associated multiple island formation must depend on the conditions on both sides of the boundary, as shown by studies of asymmetric spontaneous reconnection [e.g., *Cassak and Shay*, 2007; *Birn et al.*, 2010]. Moreover, the density jump across the shear layer may largely change the internal structure of the vortex since the difference in the mixing speed between ions and electrons is expected to produce charge separation within the vortex. This charge separation may affect plasma mixing or acceleration within the vortex. Thus, particle simulation study considering actual asymmetries across the shear layer is necessary as a next step of this study. Recent Vlasov simulations in the transverse case with moderate asymmetries of density and temperature have successfully reproduced the formation of MHD-scale KH vortices, with much smaller numerical noise than particle simulations [*Umeda et al.*, 2010]. While Vlasov simulations including in-plane magnetic field component cannot be performed on the present computer resource, the next generation supercomputer will enable us to perform such Vlasov simulations with actual asymmetries taken into account.

[52] Three-dimensional effects also may affect the VIR and should not be neglected. Recent three-dimensional MHD simulations have shown that the three-dimensional magnetotail structure, with the KH unstable low-latitude region sandwiched between KH stable high-latitude regions, can largely affect the KHI development [e.g., *Takagi et al.*, 2006]. In addition, the variation along the Z direction may allow the mode conversion between the KH waves and the kinetic Alfvén waves (KAWs) [*Chaston et al.*, 2007]. The KAWs also could be important for plasma mixing and field-aligned electron acceleration. The variation along Z direction may also allow electron beam instabilities and associated electrostatic solitary waves (ESWs) to be excited within the vortex [e.g., *Umeda et al.*, 2004], since the VIR produces beam-like accelerated electrons streaming in the Z direction within the vortex, as shown in Figures 15c and 15d. Such instabilities may affect the structure of the vortex itself. The next generation supercomputer will enable us to study these three-dimensional effects using three-dimensional particle simulations of the MHD-scale KH vortex.

[53] Although only $L_X = \lambda_{KH}$ cases are treated in this study, when the system size is large enough for multiple vortices to appear ($L_X \gg \lambda_{KH}$), it is well known in a hydrodynamic system that the coalescence (pairing) of the multiple vortices occurs, and consequently the size of the vortices becomes larger through the coalescence process. *Nakamura and Fujimoto* [2008] have revealed, using two-fluid simulations, that the (type I) VIR allows the coalescence process to progress continuously without being suppressed by the in-plane magnetic field. We revealed in section 3.6 that the growth of the VIR is assisted by the ion kinetic effects when the minimum half thickness of the compressed current sheet d_{min} is smaller than ρ_i. Since d_{min} tends to become smaller with decreasing the vortex size λ_{KH} (see Figure 8), the ion kinetic effects could mainly affect the earlier stage of a series of the coalescence process. On the other hand, in terms of electron acceleration via the VIR, electron kinetic effects may be important in the interaction of multiple vortices. This is because the coexistence of multiple vortices could allow electrons accelerated at a VIR region to be further accelerated at other VIR regions; this process may be repeated as long as the coalescence continues. Such a Fermi-type particle acceleration process via the VIR may play some roles in particle acceleration in MHD-scale turbulence induced by the KH-like flow driven instability. Thus, to universally understand the MHD-scale development of the KH vortex, the interaction of multiple vortices should not be neglected.

[54] While this study treats only Earth-like MHD-scale ($D_0 \geq \lambda_i > \rho_i$) cases, non-MHD-scale cases ($D_0 < \lambda_i$) may also be important from a comparative planetology point of view. Indeed, the MESSENGER spacecraft has recently reported the generation of KH vortices even at the ion-kinetic-scale Mercury's magnetopause [*Boardsen et al.*, 2010]. Recent particle simulations in the transverse case have shown that such an ion-kinetic-scale velocity shear layer tends to broaden by the finite ion Larmor radius effect [*Nakamura et al.*, 2010]. *Nakamura et al.* [2010] suggested that this shear layer broadening can lead to a large dawn-dusk asymmetry in the evolution of KH vortices. In addition, we revealed in this study that the number of magnetic island generated in the compressed current sheet decreases as D_0 decreases. Therefore, in Mercury-like ion-kinetic-scale situations, even one island may not appear, that is, only single X line could appear in the compressed current sheet. Thus, there could be large differences in the nature of the KH vortex between the Earth-like MHD-scale and Mercury-like ion-kinetic-scale situations.

[55] Finally, while only small ion-to-electron mass ratio ($M = 25, 100$) cases are treated in this study, in the near future, larger mass ratio cases should be performed to understand the exact VIR physics. The survey on the mass ratio may be important especially when the KHI growth rate is extremely large ($V_0/D_0 > 1.5$), since the current sheet thinning stops at the time when the current sheet thickness reaches the electron inertial length $\lambda_e(\sim\sqrt{1/M}\lambda_i)$. In addition, in such situations, since the thinning stops before the growth rate of the tearing instability becomes comparable to that of the KHI, the physics of the VIR may depend mainly

on the driven (forced) reconnection process, not on the tearing instability. Note for example that previous MHD studies showed that the tearing instability can never appear in the VIR process [e.g., *Hofman*, 1975], although our kinetic study reveals that when $V_0/D_0 < 1.5$, the tearing instability can play an important role in the VIR process (section 3.3).

References

Birn, J., et al. (2001), Geospace Environmental Modeling (GEM) Magnetic Reconnection Challenge, *J. Geophys. Res.*, *106*, 3715.

Birn, J., J. E. Borovsky, M. Hesse, and K. Schindler (2010), Scaling of asymmetric reconnection in compressible plasmas, *Phys. Plasmas*, *17*, 052108, doi:10.1063/1.3429676.

Boardsen, S. A., T. Sundberg, J. A. Slavin, B. J. Anderson, H. Korth, S. C. Solomon, and L. G. Blomberg (2010), Observations of Kelvin-Helmholtz waves along the dusk-side boundary of Mercury's magnetosphere during MESSENGER's third flyby, *Geophys. Res. Lett.*, *37*, L12101, doi:10.1029/2010GL043606.

Cai, D., R. O. Storey, and T. Neubert (1990), Kinetic equilibria of plasma shear layers, *Phys. Fluids B*, *2*, 75, doi:10.1063/1.859541.

Cassak, P. A., and M. A. Shay (2007), Scaling of asymmetric magnetic reconnection: General theory and collisional simulations, *Phys. Plasmas*, *14*, 102114, doi:10.1063/1.2795630.

Chacón, L., D. A. Knoll, and J. M. Finn (2003), Hall MHD effects on the 2D Kelvin-Helmholtz tearing instability, *Phys. Lett. A*, *308*, 187, doi:10.1016/S0375-9601(02)01807-8.

Chandrasekhar, S. (1961), *Hydrodynamic and Hydromagnetic Stability*, Oxford Univ. Press, New York.

Chaston, C. C., M. Wilber, F. S. Mozer, M. Fujimoto, M. L. Goldstein, M. Acuna, H. Reme, and A. Fazakerley (2007), Mode conversion and anomalous transport in Kelvin-Helmholtz vortices and kinetic Alfvén waves at the Earth's magnetopause, *Phys. Rev. Lett.*, *99*, 175004, doi:10.1103/PhysRevLett.99.175004.

Cowee, M. M., D. Winske, and S. P. Gary (2009), Two-dimensional hybrid simulations of superdiffusion at the magnetopause driven by Kelvin-Helmholtz instability, *J. Geophys. Res.*, *114*, A10209, doi:10.1029/2009JA014222.

Drake, J. F., M. Swisdak, H. Che, and M. A. Shay (2006), Electron acceleration from contracting magnetic islands during reconnection, *Nature*, *443*, 553, doi:10.1038/nature05116.

Dungey, J. W. (1955), Electrodynamics of the outer atmosphere, in *Proceedings of the Conference of the Ionosphere*, p. 225, Phys. Soc., London.

Fairfield, D. H., A. Otto, T. Mukai, S. Kokubun, R. P. Lepping, J. T. Steinberg, A. J. Lazarus, and T. Yamamoto (2000), Geotail observations of Kelvin-Helmholtz instability at the equatorial magnetotail boundary for parallel northward fields, *J. Geophys. Res.*, *105*, 21,159, doi:10.1029/1999JA000316.

Fujimoto, M., and T. Terasawa (1994), Anomalous ion mixing within an MHD scale Kelvin-Helmholtz vortex, *J. Geophys. Res.*, *99*, 8601, doi:10.1029/93JA02722.

Fujimoto, M., T. Mukai, H. Kawano, M. Nakamura, A. Nishida, Y. Saito, T. Yamamoto, and S. Kokubun (1998), Structure of the low-latitude boundary layer: A case study with Geotail data, *J. Geophys. Res.*, *103*, 2297, doi:10.1029/97JA02946.

Ganguli, G., Y. C. Lee, and P. Palmadesso (1988), Kinetic theory for electrostatic waves due to transverse velocity shears, *Phys. Fluids*, *31*, 823, doi:10.1063/1.866818.

Hasegawa, H., M. Fujimoto, K. Maezawa, Y. Saito, and T. Mukai (2003), Geotail observations of the dayside outer boundary region: Interplanetary magnetic field control and dawn-dusk asymmetry, *J. Geophys. Res.*, *108*(A4), 1163, doi:10.1029/2002JA009667.

Hasegawa, H., M. Fujimoto, T.-D. Phan, H. Rème, A. Balogh, M. W. Dunlop, C. Hashimoto, and R. TanDokoro (2004a), Transport of solar wind into Earth's magnetosphere through rolled-up Kelvin-Helmholtz vortices, *Nature*, *430*, 755, doi:10.1038/nature02799.

Hasegawa, H., M. Fujimoto, Y. Saito, and T. Mukai (2004b), Dense and stagnant ions in the low-latitude boundary region under northward inter-

planetary magnetic field, *Geophys. Res. Lett.*, *31*, L06802, doi:10.1029/2003GL019120.

Hasegawa, H., M. Fujimoto, K. Takagi, Y. Saito, T. Mukai, and H. Rème (2006), Single-spacecraft detection of rolled-up Kelvin-Helmholtz vortices at the flank magnetopause, *J. Geophys. Res.*, *111*, A09203, doi:10.1029/2006JA011728.

Hasegawa, H., et al. (2009), Kelvin-Helmholtz waves at the Earth's magnetopause: Multiscale development and associated reconnection, *J. Geophys. Res.*, *114*, A12207, doi:10.1029/2009JA014042.

Hofman, I. (1975), Resistive tearing modes in a sheet pinch with shear flow, *Plasma Phys.*, *17*, 143, doi:10.1088/0032-1028/17/2/005.

Hoshino, M. (2005), Electron surfing acceleration in magnetic reconnection, *J. Geophys. Res.*, *110*, A10215, doi:10.1029/2005JA011229.

Hoshino, M., T. Mukai, T. Terasawa, and I. Shinohara (2001), Suprathermal electron acceleration in magnetic reconnection, *J. Geophys. Res.*, *106*, 25,979, doi:10.1029/2001JA900052.

Knoll, D. A., and L. Chacón (2002), Magnetic reconnection in the two-dimensional Kelvin-Helmholtz instability, *Phys. Rev. Lett.*, *88*, 215003, doi:10.1103/PhysRevLett.88.215003.

Matsumoto, Y., and M. Hoshino (2006), Turbulent mixing and transport of collisionless plasmas across a stratified velocity shear layer, *J. Geophys. Res.*, *111*, A05213, doi:10.1029/2004JA010988.

Mitchell, D. G., F. Kutchko, D. J. Williams, T. E. Eastman, L. A. Frank, and C. T. Russell (1987), An extended study of the low-latitude boundary layer on the dawn and dusk flanks of the magnetosphere, *J. Geophys. Res.*, *92*, 7394, doi:10.1029/JA092iA07p07394.

Miura, A. (1984), Anomalous transport by magnetohydrodynamic Kelvin-Helmholtz instabilities in the solar wind-magnetosphere interaction, *J. Geophys. Res.*, *89*, 801, doi:10.1029/JA089iA02p00801.

Miura, A. (1987), Simulation of Kelvin-Helmholtz instability at the magnetospheric boundary, *J. Geophys. Res.*, *92*, 3195, doi:10.1029/JA092iA04p03195.

Miura, A., and P. L. Pritchett (1982), Nonlocal stability analysis of the MHD Kelvin-Helmholtz instability in a compressible plasma, *J. Geophys. Res.*, *87*, 7431, doi:10.1029/JA087iA09p07431.

Nakamura, T. K. M., and M. Fujimoto (2005), Magnetic reconnection rolled-up MHD-scale Kelvin-Helmholtz vortices: Two-fluid simulations including finite electron inertial effects, *Geophys. Res. Lett.*, *32*, L21102, doi:10.1029/2005GL023362.

Nakamura, T. K. M., and M. Fujimoto (2008), Magnetic effects on the coalescence of Kelvin-Helmholtz vortices, *Phys. Rev. Lett.*, *101*, 165002, doi:10.1103/PhysRevLett.101.165002.

Nakamura, T. K. M., D. Hayashi, M. Fujimoto, and I. Shinohara (2004), Decay of MHD-scale Kelvin-Helmholtz vortices medicated by parasitic electron dynamics, *Phys. Rev. Lett.*, *92*, 145001, doi:10.1103/PhysRevLett.92.145001.

Nakamura, T. K. M., M. Fujimoto, and A. Otto (2006), Magnetic reconnection induced by weak Kelvin-Helmholtz instability and the formation of the low-latitude boundary layer, *Geophys. Res. Lett.*, *33*, L14106, doi:10.1029/2006GL026318.

Nakamura, T. K. M., M. Fujimoto, and A. Otto (2008), Structure of an MHD-scale Kelvin-Helmholtz vortex: Two-dimensional two-fluid simulations including finite electron inertial effects, *J. Geophys. Res.*, *113*, A09204, doi:10.1029/2007JA012803.

Nakamura, T. K. M., H. Hasegawa, and I. Shinohara (2010), Kinetic effects on the Kelvin-Helmholtz instability in ion-to-MHD scale transverse velocity shear layers: Particle simulations, *Phys. Plasmas*, *17*, 042119, doi:10.1063/1.3385445.

Nykyri, K., and A. Otto (2001), Plasma transport at the magnetospheric boundary due to reconnection in Kelvin-Helmholtz vortices, *Geophys. Res. Lett.*, *28*, 3565, doi:10.1029/2001GL013239.

Opp, E. N., and A. B. Hassam (1991), Kelvin-Helmholtz instability in systems with large effective Larmor radius, *Phys. Fluids B*, *3*, 885, doi:10.1063/1.859845.

Otto, A., and D. H. Fairfield (2000), Kelvin-Helmholtz instability at the magnetotail boundary: MHD simulation and comparison with Geotail observations, *J. Geophys. Res.*, *105*, 21,175, doi:10.1029/1999JA000312.

Pei, W., R. Horiuchi, and T. Sato (2001a), Long time evolution of collisionless driven reconnection in a two-dimensional open system, *Phys. Plasmas*, *8*, 3251, doi:10.1063/1.1375150.

Pei, W., R. Horiuchi, and T. Sato (2001b), Ion dynamics in steady collisionless driven reconnection, *Phys. Rev. Lett.*, *87*, 235003, doi:10.1103/PhysRevLett.87.235003.

Phan, T. D., et al. (1997), Low-latitude dusk flank magnetosheath, magnetopause, and boundary layer for low magnetic shear: Wind observations, *J. Geophys. Res.*, *102*, 19,883, doi:10.1029/97JA01596.

Pritchett, P. L., and F. V. Coroniti (1984), The collisionless macroscopic Kelvin-Helmholtz instability: 1. Transverse electrostatic mode, *J. Geophys. Res.*, *89*, 168, doi:10.1029/JA089iA01p00168.

Pritchett, P. L., and F. V. Coroniti (2004), Three-dimensional collisionless magnetic reconnection in the presence of a guide field, *J. Geophys. Res.*, *109*, A01220, doi:10.1029/2003JA009999.

Pu, Z. Y., M. Yei, and Z. X. Liu (1990), Generation of vortex-induced tearing mode instability at the magnetopause, *J. Geophys. Res.*, *95*, 10,559, doi:10.1029/JA095iA07p10559.

Sckopke, N., G. Paschmann, G. Haerendel, B. U. Ö. Sonnerup, S. J. Bame, T. G. Forbes, E. W. Hones Jr., and C. T. Russell (1981), Structure of the low-latitude boundary layer, *J. Geophys. Res.*, *86*, 2099, doi:10.1029/JA086iA04p02099.

Slavin, J. A., et al. (2008), Mercury's magnetosphere after MESSENGER's first flyby, *Science*, *321*, 85, doi:10.1126/science.1159040.

Slavin, J. A., et al. (2009), MESSENGER observations of Mercury's magnetosphere during northward IMF, *Geophys. Res. Lett.*, *36*, L02101, doi:10.1029/2008GL036158.

Song, P., and C. T. Russell (1992), Model of the formation of the low-latitude boundary layer for strongly northward interplanetary magnetic field, *J. Geophys. Res.*, *97*, 1411, doi:10.1029/91JA02377.

Takagi, K., C. Hashimoto, H. Hasegawa, M. Fujimoto, and R. TanDokoro (2006), Kelvin-Helmholtz instability in a magnetotail flank-like geometry: Three-dimensional MHD simulations, *J. Geophys. Res.*, *111*, A08202, doi:10.1029/2006JA011631.

Umeda, T., Y. Omura, and H. Matsumoto (2004), Two-dimensional particle simulation of electromagnetic field signature associated with electrostatic solitary waves, *J. Geophys. Res.*, *109*, A02207, doi:10.1029/2003JA010000.

Umeda, T., J. Miwa, Y. Matsumoto, T. K. M. Nakamura, K. Togano, K. Fukazawa, and I. Shinohara (2010), Full electromagnetic Vlasov code simulation of the Kelvin-Helmholtz instability, *Phys. Plasmas*, *17*, 052311, doi:10.1063/1.3422547.

M. Fujimoto, H. Hasegawa, T. K. M. Nakamura, and I. Shinohara, Institute of Space and Astronautical Science, JAXA, Sagamihara, Kanagawa 252-5210, Japan. (takuma@stp.isas.jaxa.jp)